

AD-A046 048

OHIO STATE UNIV COLUMBUS ELECTROSCIENCE LAB
AN MM-8TD ANALYSIS OF THE RADIATION FROM SLOTS IN PLANAR AND CY--ETC(U)
JUL 77 P H PATHAK, J HUANG
ESL-4396-1

F/G 20/14

F19628-76-C-0154

NL

RADC-TR-77-242

UNCLASSIFIED

OF

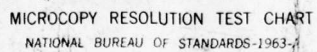
AD
A046048



END
DATE
FILMED

11-77

DDC



MICROCOPY RESOLUTION TEST CHART
NATIONAL BUREAU OF STANDARDS-1963-A

RADC-TR-77-242
Interim Technical Report
July 1977

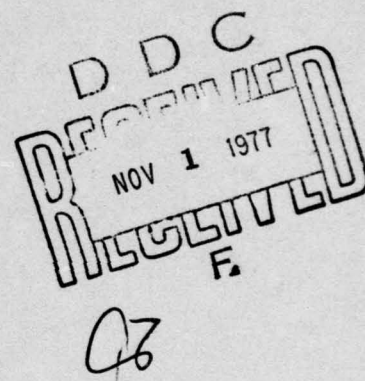
12
B.S.



AN MM-GTD ANALYSIS OF THE RADIATION FROM SLOTS IN PLANAR
AND CYLINDRICAL PERFECTLY-CONDUCTING STRUCTURES WITH
A SURFACE IMPEDANCE PATCH

P. H. Pathak and J. Huang

AD A 046048



INTERIM TECHNICAL REPORT 4396-1

July 1977

Approved for public release;
distribution unlimited

AD No. _____
DDC FILE COPY

ROME AIR DEVELOPMENT CENTER
AIR FORCE SYSTEMS COMMAND
GRIFFISS AIR FORCE BASE, NEW YORK 13441

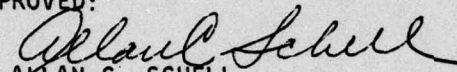
This report has been reviewed by the RADC Information Office (OI) and is releasable to the National Technical Information Service (NTIS). At NTIS it will be releasable to the general public, including foreign nations.

This technical report has been reviewed and approved for publication.

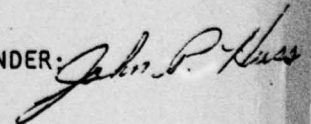
APPROVED:


NICHOLAS P. KERNWEIS
Project Engineer

APPROVED:


ALLAN C. SCHELL
Acting Chief
Electromagnetic Sciences Division

FOR THE COMMANDER:



Plans Office

UNCLASSIFIED

SECURITY CLASSIFICATION OF THIS PAGE (When Data Entered)

19 REPORT DOCUMENTATION PAGE		READ INSTRUCTIONS BEFORE COMPLETING FORM
1. REPORT NUMBER RADC-TR-77-242 ✓	2. GOVT ACCESSION NO.	3. RECIPIENT'S CATALOG NUMBER
4. TITLE (and Subtitle) AN MM-GTD ANALYSIS OF THE RADIATION FROM SLOTS IN PLANAR AND CYLINDRICAL PERFECTLY-CONDUCTING STRUCTURES WITH A SURFACE IMPEDANCE PATCH,	5. TYPE OF REPORT & PERIOD COVERED Scientific Report No. 1	6. PERFORMING ORG. REPORT NUMBER ESL-4396-1, Scientific-1
7. AUTHOR(S) P. H./Pathak and J./Huang	8. CONTRACT OR GRANT NUMBER(S) Contract F19628-76-C-0154 ✓	
9. PERFORMING ORGANIZATION NAME AND ADDRESS The Ohio State University ElectroScience Laboratory, Department of Electrical Engineering Columbus, Ohio 43212	10. PROGRAM ELEMENT, PROJECT, TASK AREA & WORK UNIT NUMBERS	
11. CONTROLLING OFFICE NAME AND ADDRESS Deputy for Electronic Technology (RADC/ETER) ✓ Hanscom AFB, MA 01731 Contract Monitor: Nicholas P. Kernweis, ETER	12. REPORT DATE Jul 1977	13. NUMBER OF PAGES 54
14. MONITORING AGENCY NAME & ADDRESS (if different from Controlling Office) Interim technical rept.,	15. SECURITY CLASS. (of this report) Unclassified	15a. DECLASSIFICATION/DOWNGRADING SCHEDULE
16. DISTRIBUTION STATEMENT (of this Report) Approved for public release; distribution unlimited		
17. DISTRIBUTION STATEMENT (of the abstract entered in Block 20, if different from Report)		
18. SUPPLEMENTARY NOTES		
19. KEY WORDS (Continue on reverse side if necessary and identify by block number) Antennas on an impedance surface Perturbation type integral equation Method of Moments (MM) Geometrical Theory of Diffraction (GTD) MM-GTD		
20. ABSTRACT (Continue on reverse side if necessary and identify by block number) The radiation from a slot in an electrically large, perfectly conducting cylinder partly covered with an impedance surface is treated by a combination of the geometrical theory of diffraction (GTD) and the method of moments (MM). The method is far more efficient than MM solutions of conventional integral equations because a perturbation type integral equation which requires the unknown to be evaluated only over the impedance patch is employed in the present analysis. Furthermore, the GTD method can be systematically incorporated into this perturbation integral equation not only to provide substantial		

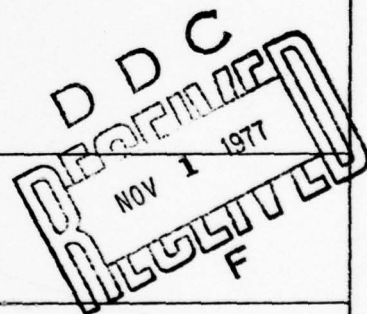
DD FORM 1 JAN 73 1473

EDITION OF 1 NOV 65 IS OBSOLETE

UNCLASSIFIED

SECURITY CLASSIFICATION OF THIS PAGE (When Data Entered)

402 251



UNCLASSIFIED

SECURITY CLASSIFICATION OF THIS PAGE(When Data Entered)

20.

simplifications in the solution, but also to directly treat convex cylinders of variable curvature.

Numerical results are presented for the two-dimensional circular cylinder case for different size cylinders, different surface impedance values, and for different size surface impedance patches. The radiation from slots in an infinite, planar perfectly-conducting surface which is partly covered with an impedance surface is also analyzed via the MM-GTD solution of the same perturbation type integral equation as in the cylinder case. A comparison of the antenna pattern calculations for the planar and cylindrical configurations indicates the effects of surface curvature especially in the region of space in which the slot is directly visible.

ACCESSION for	
NTS	File Section <input checked="" type="checkbox"/>
DDC	B ff Section <input type="checkbox"/>
J S I G A T	
BY	
SUBSCRIPTION/AVAILABILITY CODES	
ON	SPECIAL
A	

ii

UNCLASSIFIED

SECURITY CLASSIFICATION OF THIS PAGE(When Data Entered)

ACKNOWLEDGMENT

The authors wish to thank Professors J. H. Richmond and L. Peters, Jr. for many stimulating discussions. Thanks are also due to Dr. W. D. Burnside for providing the pattern in Figure 24 which is based on the MM-GTD solution of the conventional electric field integral equation (EFIE).

TABLE OF CONTENTS

	Page
I INTRODUCTION	1
II ANALYTICAL FORMULATION	5
III NUMERICAL RESULTS AND DISCUSSION	30
REFERENCES	54

Preceding Page BLANK - NOT FILMED

I. INTRODUCTION

This report deals with an analysis of the high frequency (h.f.) radiation from slots in planar and cylindrical, perfectly-conducting surfaces which are partly covered with an impedance surface patch. The present study is applicable to the problem of controlling the polarization and pattern shape of the electromagnetic radiation from a flush mounted airborne antenna for satellite communication purposes. In this application, a slot antenna is flush mounted in the aircraft fuselage, and one is interested in the radiation pattern in the roll plane containing the antenna. Thus, the problem is essentially two-dimensional (2-D) in nature, and the aircraft fuselage may be approximately modeled by a circular cylinder in the roll plane. The aircraft wing structure is ignored in this initial study; however, its effects can be readily incorporated in the future via the geometrical theory of diffraction (GTD) as will be discussed later on. In particular, the behavior of the radiated fields in the vicinity of the horizon (or the shadow boundary) associated with the antenna are of prime interest in the satellite communication type application. Thus, it is desirable for the airborne antenna to have a gain approximately that of the pattern maximum near the horizon; such a desired high gain may be achieved by an impedance surface type of loading around the slot.

Figures 1 and 2 illustrate the antenna configurations of interest which are analyzed in this report. The slot is present in the perfectly-conducting surface and the perfectly-conducting surface is coated with a sufficiently long impedance surface patch which also covers the slot as indicated in Figures 1 and 2. With a proper choice of the impedance, the slot may be allowed to radiate like an end-fire surface wave type antenna near the horizon; it is this end-fire effect which may be employed to increase the gain near the horizon. By a proper choice of the impedance, it is implied that the type of impedance chosen is such that it supports a bound surface wave mode on the planar impedance surface of Figure 1; whereas, it supports an Elliot type mode [1] on the curved impedance surface of Figure 2. The Elliot mode propagates along the curved impedance surface with negligible attenuation or leakage, and it corresponds in the limiting case of the infinite radius of curvature to the bound surface wave mode which exists on the planar impedance surface. It is noted that these surface wave type modes are excited by an axial slot in the configurations of Figures 1 and 2, if the surface impedance is inductive. On the other hand, the circumferential slot will excite these modes only if the surface impedance is capacitive. These surface wave modes on the impedance surface diffract from the ends of the impedance patch (as a result of the discontinuity in surface impedance there), thereby producing an end-fire effect.

While the cylindrical antenna configuration of Figure 2 is important in this study because it models an aircraft fuselage in the roll plane, the planar configuration of Figure 1 is also analyzed in this report

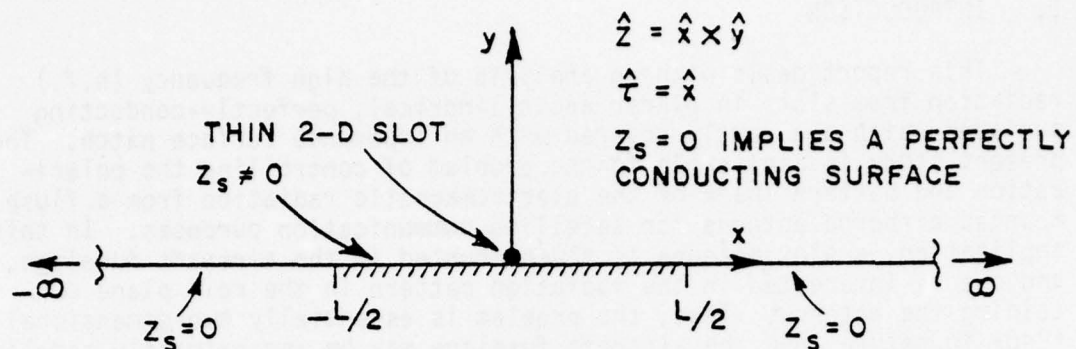


Figure 1. A thin, 2-D slot in an infinitely long, planar, perfectly-conducting structure with a surface impedance patch of length L . The value of the surface impedance is Z_s .

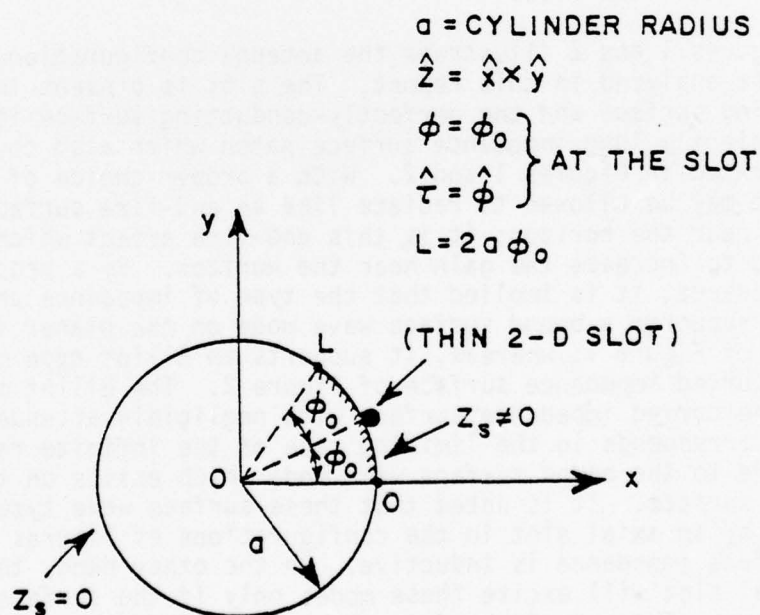


Figure 2. A thin, 2-D slot in a perfectly-conducting circular cylinder with a surface impedance patch of arc length, L . The value of the surface impedance is Z_s .

because it is a more basic geometrical configuration involving a perfectly-conducting structure with a surface impedance patch, and because a comparison of the patterns for the configurations in Figures 1 and 2 allows one to ascertain the effects of surface curvatures on the patterns especially in the region of space in which the slot is directly visible.

In the present analysis, the impedance surface patch is used to approximately simulate the effects of a thin, uniform dielectric or ferrite cover or properly designed corrugated surface of finite extent on the perfectly-conducting planar or cylindrical antenna structure. The slot in the perfectly-conducting structure is covered by the dielectric or ferrite material, and it is assumed that the electric field in the slot aperture is known, so that one also knows the equivalent magnetic current in the aperture. It is noted that the equivalent magnetic current in the aperture of the slot is \hat{z} -directed for the 2-D axial slot, whereas it is \hat{r} -directed for the 2-D circumferential slot. Hence, the axial slot may be referred to as a \hat{z} -directed slot, and the circumferential slot may be likewise referred to as a \hat{r} -directed slot. The radiation from a slot of finite width may be obtained by quantizing the source distribution in the aperture, and by superposing the fields radiated by each of the quantized sources. An equivalent quantized source in this case is a \hat{z} -directed magnetic line source for the axial slot, whereas, it is a \hat{r} -directed magnetic line dipole for the circumferential slot. These equivalent quantized magnetic currents radiate in the presence of the perfectly-conducting surface (which covers the aperture as well), and in the presence of the dielectric or ferrite material which covers the perfectly-conducting surface. The strengths of the equivalent sources are weighted according to the source distribution in the aperture. In the present report, only the radiation from a magnetic line source and a magnetic line dipole will be analyzed since the radiation from a slot of finite width may be readily obtained from this analysis by superposition. In the impedance surface approximation for the truncated dielectric or ferrite cover on the perfectly-conducting surface, the equivalent problem to be analyzed consists of an equivalent magnetic line or line dipole source on the impedance surface patch which covers the perfectly-conducting planar or cylindrical surface.

In the absence of any surface impedance patch, the axial slot in an electrically large perfectly-conducting convex cylinder would radiate fields which are substantially stronger in the vicinity of the horizon than those radiated by a circumferentially directed slot at the same location. In fact, the difference in the power radiated by these two slots could be as much as 20 dB or so in the neighborhood of the horizon; and, in the deep shadow region this difference continues to increase significantly. The axially directed slot in a convex cylinder radiates a ϕ -directed electric field; on the other hand, the circumferential slot radiates only a \hat{z} -directed electric field in the roll plane. Thus, the electric field components radiated by the two slots are polarized orthogonal to each other. It is observed that an alternate geometry that could prove interesting is the electric line source placed on an impedance surface. This source would in general excite a loosely bound surface wave more strongly than a magnetic line dipole source.

In some satellite communication type airborne antenna applications, it is commonly desirable for the axial and circumferential slots to be used in combination as a crossed slot antenna for the purposes of transmitting or receiving a circularly polarized (CP) wave near the horizon. However, the 20 dB or so difference in the power radiated individually by the two slots makes the crossed-slot configuration not too well receptive to a CP wave (or by reciprocity, the crossed-slot does not effectively radiate a CP wave) near the horizon. The present analysis could be used to ascertain if one could enhance the circumferential slot radiation near the horizon via the end-fire effect by employing a capacitive type surface impedance patch around the slot (as in Figure 2), while simultaneously not degrading the level of the radiation pattern of the axial slot component in the crossed slot configuration.

The antenna problems in Figures 1 and 2 are analyzed in this report via a combination of the method of moments (MM) and the GTD; this combination will be referred to as the MM-GTD method. An integral equation is formulated for the "scattering problem" in which the unknown tangential magnetic field induced on the surface of Figures 1 and 2 by a distant source needs to be evaluated only over the surface impedance patch. In this scattering problem, the equivalent magnetic line or line dipole source (corresponding to each of the quantized equivalent currents in the slot antenna problem) is turned off.

Since the unknown needs to be evaluated only over the surface impedance patch, one is able to treat electrically large cylinders and infinite planar structures (of Figures 2 and 1) far more efficiently than by MM solutions of conventional integral equations employing the free space Green's function, in which the unknown must be evaluated over the perfectly conducting portion of the surface as well. The source term in this integral equation represents the tangential magnetic field induced (by the distant source) on the same surface, but in the absence of the surface impedance loading, i.e., on the "unperturbed" or completely perfectly conducting surface. The kernel of this integral equation represents the tangential magnetic field which is excited on the "unperturbed" surface due to an appropriate magnetic line source on the same surface. Since the source term and the kernel of this integral equation correspond to the unperturbed or the perfectly-conducting surface without the surface impedance patch, they are readily calculated via the special Green's functions for the planar and circular perfectly conducting surfaces. Furthermore, when the asymptotic high frequency (or the GTD) approximations are employed for the cylinder Green's functions, one is able to analyze not only electrically large circular cylinders more efficiently, but also arbitrary, convex, perfectly-conducting cylinders with an impedance patch.

The unknown surface field is solved for via the usual MM procedure over just the surface impedance patch region. Once this unknown induced surface magnetic field is determined in the "scattering" problems, it also directly furnishes the radiation patterns for the "antenna" configurations of Figures 1 and 2 via reciprocity.

The analytical details are presented in Section II where it is indicated that the circumferential slot case presents certain numerical difficulties; a few approaches for circumventing these difficulties are proposed, and some preliminary numerical results for both the axial and the circumferential slot cases are presented in Section III.

II. ANALYTICAL FORMULATION

The solutions to the antenna problems of Figures 1 and 2 are formulated indirectly in terms of the solutions to their corresponding scattering problems via reciprocity, as indicated below. This formulation is presented for the 3-D case, and it is subsequently specialized to the 2-D case which is of interest.

Consider a surface S on which is placed an infinitesimal magnetic current moment \bar{M}_a at Q' as shown in Figure 3. \bar{M}_a is tangential to

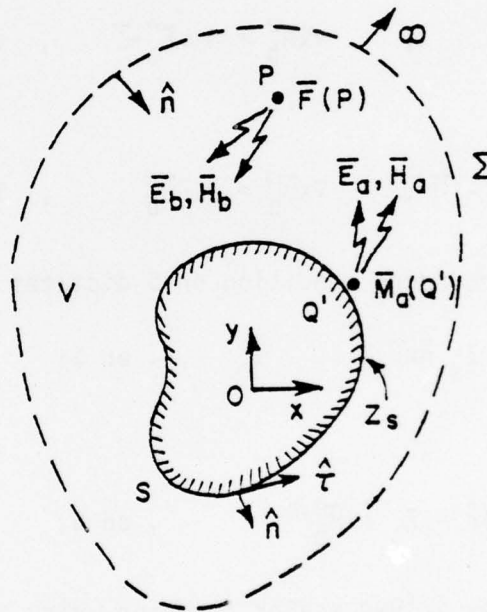


Figure 3. An illustration of the antenna and corresponding scattering problems.

S at Q' . The equivalent source \bar{M}_a generates the electromagnetic fields \bar{E}_a, \bar{H}_a in the presence of S , and it constitutes the antenna problem similar to that in Figures 1 and 2. Consider another infinitesimal current source \bar{F} at point P which is external to S ; the vector \bar{F} could represent either an infinitesimal electric current moment \bar{J} , or an infinitesimal magnetic current moment \bar{M} . The source \bar{M}_a in the antenna

problem generates \bar{E}_a, \bar{H}_a with the source \bar{F} turned off. On the other hand, \bar{F} generates the electromagnetic fields \bar{E}_b, \bar{H}_b in the presence of S , but with the source \bar{M}_a turned off; thus \bar{F} constitutes the vector source for the corresponding scattering problem. All of the above fields and sources satisfy an $e^{j\omega t}$ time dependence which is assumed and suppressed in the present analysis.

Let the surface S and the surface Σ at infinity bound the volume V . The electromagnetic fields satisfy Maxwell's equations in V , and the radiation condition on Σ . In the present analysis, the electromagnetic fields are chosen to satisfy the impedance boundary condition on S . To distinguish between the fields \bar{E}_b, \bar{H}_b due to the source \bar{F} which is either \bar{J} or \bar{M} , one lets \bar{E}_b^e, \bar{H}_b^e be the fields due to \bar{J} , and \bar{E}_b^m, \bar{H}_b^m be the fields due to \bar{M} , respectively. The Maxwell's equations are

$$\nabla \times \bar{E}_a = -j\omega\mu\bar{H}_a - \bar{M}_a; \quad \nabla \times \bar{H}_a = j\omega\epsilon\bar{E}_a, \quad (1a;1b)$$

$$\nabla \times \bar{E}_b^e = -j\omega\mu\bar{H}_b^e; \quad \nabla \times \bar{H}_b^e = j\omega\epsilon\bar{E}_b^e + \bar{J}, \quad \text{if } \bar{F}=\bar{J} \quad (2a;2b)$$

and

$$\nabla \times \bar{E}_b^m = -j\omega\mu\bar{H}_b^m - \bar{M}; \quad \nabla \times \bar{H}_b^m = j\omega\epsilon\bar{E}_b^m, \quad \text{if } \bar{F}=\bar{M}. \quad (3a;3b)$$

The impedance boundary condition on S dictates that

$$\bar{E}_a - (\bar{E}_a \cdot \hat{n})\hat{n} = Z_s \hat{n} \times \bar{H}_a, \quad \text{on } S; \quad (4a)$$

and likewise

$$\bar{E}_b^{e,m} - (\bar{E}_b^{e,m} \cdot \hat{n})\hat{n} = Z_s \hat{n} \times \bar{H}_b^{e,m}, \quad \text{on } S, \quad (4b)$$

where Z_s is a complex valued scalar function which denotes the value of surface impedance; the value of Z_s could vanish over a part of S ($Z_s = 0$ implies a perfectly conducting surface). From Equations (1) and (2), one may obtain

$$\nabla \cdot [\bar{E}_a \times \bar{H}_b^e - \bar{E}_b^e \times \bar{H}_a] = -\bar{H}_b^e \cdot \bar{M}_a - \bar{E}_a \cdot \bar{J}; \quad \text{if } \bar{F}=\bar{J}. \quad (5)$$

Similarly, one obtains from Equations (1) and (3) the following

$$\nabla \cdot (\bar{E}_a \times \bar{H}_b^m - \bar{E}_b^m \times \bar{H}_a) = -\bar{H}_b^m \cdot \bar{M}_a + \bar{H}_a \cdot \bar{M}; \quad \text{if } \bar{F}=\bar{M}. \quad (6)$$

Integration of both sides of Equations (5) and (6) over the volume V , and an application of the divergence theorem yields:

$$-\oint_S [\vec{E}_a \times \vec{H}_b^e - \vec{E}_b^e \times \vec{H}_a] \cdot \hat{n} ds = - \iiint_V [\vec{H}_b^e \cdot \vec{M}_a + \vec{E}_a \cdot \vec{J}] dv ; \text{ if } \vec{F}=\vec{J} \quad (7)$$

and

$$-\oint_S [\vec{E}_a \times \vec{H}_b^m - \vec{E}_b^m \times \vec{H}_a] \cdot \hat{n} ds = - \iiint_V [\vec{H}_b^m \cdot \vec{M}_a - \vec{H}_a \cdot \vec{M}] dv ; \text{ if } \vec{F}=\vec{M}. \quad (8)$$

The contributions to the integrals from the surface Σ at infinity vanish via the radiation condition. The surface integrals in Equations (7) and (8) vanish via the impedance boundary condition in Equation (4) as follows:

$$[\vec{E}_a \times \vec{H}_b^{e,m} - \vec{E}_b^{e,m} \times \vec{H}_a] \cdot \hat{n} = \vec{H}_b^{e,m} \cdot (Z_s \hat{n} \times \hat{n} \times \vec{H}_a) - \vec{H}_a \cdot (Z_s \hat{n} \times \hat{n} \times \vec{H}_b^{e,m}) = 0. \quad (9)$$

The infinitesimal sources \vec{M}_a and \vec{F} may be represented as

$$\vec{M}_a = m_a \hat{t} \delta(|\vec{R} - \vec{R}_Q|) ; \quad \vec{F} = \begin{cases} \vec{J} = j \hat{u} \delta(|\vec{R} - \vec{R}_P|) & ; \text{ if } \vec{F}=\vec{J} \\ \vec{M} = m \hat{v} \delta(|\vec{R} - \vec{R}_P|) & ; \text{ if } \vec{F}=\vec{M} \end{cases} \quad (10a; 10b)$$

where the amplitudes m_a , j and m are assumed known, and δ denotes the Dirac delta function in terms of the position vector $\vec{R} = x\hat{x} + y\hat{y} + z\hat{z}$ in the 3-D coordinate space. Thus, Equations (7) and (8) become via Equations (9) and (10), the following:

$$\vec{H}_b^e(Q'|P) \cdot \hat{t} m_a = - \vec{E}_a(P|Q') \cdot \hat{u} j ; \quad \text{if } \vec{F}=\vec{J} \quad (11)$$

and

$$\vec{H}_b^m(Q'|P) \cdot \hat{t} m_a = \vec{H}_a(P|Q') \cdot \hat{v} m ; \quad \text{if } \vec{F}=\vec{M} . \quad (12)$$

The notation, $\vec{H}_b^{e,m}(Q'|P)$ implies that it is the field produced by the source at P , and evaluated or sampled at Q' . Similarly, $\vec{E}_a(P|Q')$, $\vec{H}_a(P|Q')$ are the fields due to the source at Q' , and they are evaluated or sampled at P . The quantities on the LHS of Equations (11) and (12) may be interpreted as

$$\bar{H}_b^{e,m}(Q'|P) \cdot \hat{t} m_a \equiv \lim_{Q'' \rightarrow Q'} \iiint_V \bar{H}_b^{e,m} \cdot \hat{t} m_a \delta(|\bar{R} - \bar{R}_{Q''}|) dv,$$

where the point Q'' is external to S . For the sake of convenience one lets $j \equiv 1$ (if $\bar{F} = \bar{J}$), and $m \equiv 1$ (if $\bar{F} = \bar{M}$); it is then clear that by orienting $\bar{J} = \hat{u}J$ or $\bar{M} = \hat{v}M$ along \bar{E}_a or \bar{H}_a , respectively one can calculate the fields \bar{E}_a , or \bar{H}_a of the radiation problem which are originally of interest, if the induced, tangential magnetic fields $\bar{H}_b^{e,m}(Q'|P) \cdot \hat{t}$, or $\bar{H}_b^m(Q'|P) \cdot \hat{t}$ in the scattering problem are known.

One may directly employ the three-dimensional (3-D) results developed above to the 2-D configurations of interest in which the geometry, the source, and the fields have no variation along the \hat{z} -direction. In the 2-D case, the equivalent magnetic current moment \bar{M}_a becomes a magnetic line source. For the infinitesimally thin axial (or \hat{z} -directed) slot case, the equivalent magnetic line source possesses magnetic current elements which are \hat{z} -directed, whereas in the infinitesimal circumferential (or \hat{t} -directed) slot case, the equivalent magnetic line source possesses magnetic current elements which are \hat{t} -directed so that the equivalent source is referred to as a magnetic line dipole in this case. Thus, in the 2-D infinitesimal axial slot case \bar{M}_a is given by $\bar{M}_a = \hat{z} m_a \delta(|\bar{\rho} - \bar{\rho}_{Q'}|)$, with $t = \hat{z}$, and one chooses $\bar{F} = \bar{M}$ with $\hat{v} = \hat{z}$ since the axial slot generates only a \hat{z} directed \bar{H}_a in the 2-D problem. With $m=1$, Equation (12) reduces in the 2-D case to

$$\bar{H}_a(P|Q') \cdot \hat{z} = \bar{H}_b^m(Q'|P) \cdot \hat{z} m_a \quad ; \quad \text{for the axial slot case,} \quad (13)$$

where it is noted that for $\bar{F} = \bar{M} = \hat{z} \delta(|\bar{\rho} - \bar{\rho}_P|)$, \bar{H}_b^m is also \hat{z} -directed in the 2-D problem. The $\delta(|\bar{\rho} - \bar{\rho}_{Q'}|)$ implies a 2-D delta function in the 2-D, (x,y) coordinate space with $\bar{\rho} = x\hat{x} + y\hat{y}$ in contrast to the 3-D delta functions in the (x,y,z) coordinate space as in Equations (10a;10b).

In the 2-D infinitesimal circumferential slot case, \bar{M}_a is a magnetic line dipole given by $\bar{M}_a = \hat{t} m_a \delta(|\bar{\rho} - \bar{\rho}_Q|)$ with $t = \hat{t}$ being the unit tangent vector to the 2-D boundary S in the (x,y) plane as in Figure 3, and one chooses $\bar{F} = \bar{J} = \hat{z} \delta(|\bar{\rho} - \bar{\rho}_P|)$ with $\hat{u} = \hat{z}$ and $j=1$, since \bar{M}_a now generates an \bar{E}_a which has only a \hat{z} -component in the 2-D problem. Also, \bar{E}_b^e generated by this \bar{J} is entirely \hat{z} -directed in the 2-D case. Consequently, Equation (11) becomes

$$\bar{E}_a(P|Q') \cdot \hat{z} = - \bar{H}_b^e(Q'|P) \cdot \hat{t} m_a \quad ; \quad \text{for the circumferential slot case.} \quad (14)$$

As a next step, the solution to the quantities $\vec{H}_b^m(Q'|P) \cdot \hat{z}$ of Equation (13) for the 2-D axial slot, and $\vec{H}_b^m(Q'|P) \cdot \hat{\tau}$ of Equation (14) for the 2-D circumferential slot, respectively, will be formulated in terms of integral equations for the scattering problem; and these integral equations will be numerically evaluated via the method of moments (MM), thereby also providing the solution for \vec{E}_a, \vec{H}_a of the antenna problems via Equation (13) and Equation (14) for the two different types of slots. The scattering problem corresponding to the evaluation of $\vec{H}_b^m(Q'|P) \cdot \hat{z}$ on S will be referred to as the TE_z case; whereas, that corresponding to the evaluation of $\vec{H}_b^m(Q'|P) \cdot \hat{\tau}$ on S will be referred to as the TM_z case. The formulation leading to the integral equations is first given for the 3-D case, and it is later specialized to the 2-D scattering problems of interest.

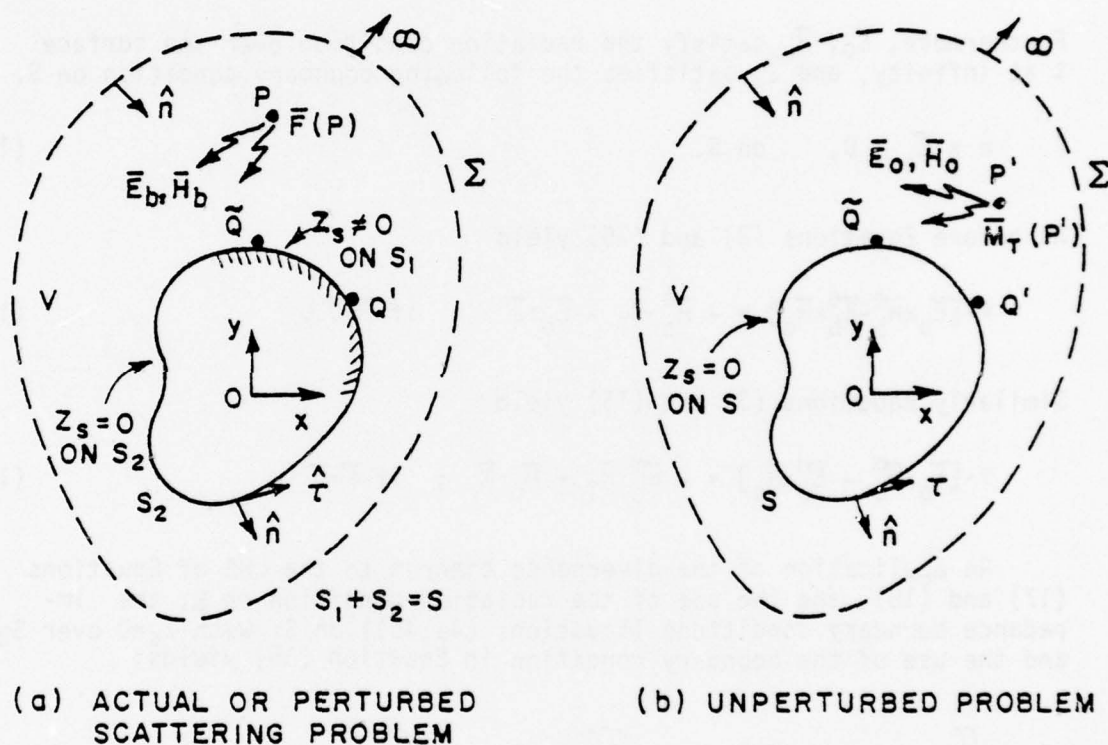


Figure 4. The actual scattering problem, and a related unperturbed problem.

Figure 4(a) illustrates the same scattering problem as in Figure 3, except that the surface impedance Z_s is now specifically taken to be nonzero on the portion S_1 , whereas, it is zero everywhere on the remaining portion S_2 of the surface S . Again the source \vec{F} may be either \vec{J} or \vec{M} , and \vec{J} radiates the fields \vec{E}_b, \vec{H}_b in the presence of S , likewise, \vec{M} radiates \vec{E}_b, \vec{H}_b as before.

The scattering problem in Figure 4(a) will be referred to as the perturbed problem due to the fact that the presence of a nonzero Z_s over S_1 may be viewed as a perturbation of the perfectly conducting surface which would otherwise have existed over the entire surface S .

Figure 4(b) illustrates the unperturbed problem in which the entire surface S is perfectly conducting. The excitation chosen for the unperturbed problem in Figure 4(b) is an infinitesimal magnetic current moment \vec{M}_T external to S which generates the fields \vec{E}_0, \vec{H}_0 in the presence of S . The fields \vec{E}_0, \vec{H}_0 satisfy Maxwell's equations

$$\nabla \times \vec{E}_0 = -j\omega\mu \vec{H}_0 - \vec{M}_T \quad ; \quad \nabla \times \vec{H}_0 = j\omega\epsilon \vec{E}_0 \quad . \quad (15a; 15b)$$

Furthermore, \vec{E}_0, \vec{H}_0 satisfy the radiation condition over the surface Σ at infinity, and \vec{E}_0 satisfies the following boundary condition on S :

$$\hat{n} \times \vec{E}_0 = 0, \quad \text{on } S. \quad (16)$$

As before Equations (2) and (15) yield

$$\nabla \cdot [\vec{E}_0 \times \vec{H}_b^e - \vec{E}_b^e \times \vec{H}_0] = -\vec{H}_b^e \cdot \vec{M}_T - \vec{E}_0 \cdot \vec{J} \quad ; \quad \text{if } \vec{F} = \vec{J}. \quad (17)$$

Similarly Equations (3) and (15) yield

$$\nabla \cdot [\vec{E}_0 \times \vec{H}_b^m - \vec{E}_b^m \times \vec{H}_0] = -\vec{H}_b^m \cdot \vec{M}_T + \vec{H}_0 \cdot \vec{M} \quad ; \quad \text{if } \vec{F} = \vec{M}. \quad (18)$$

An application of the divergence theorem to the LHS of Equations (17) and (18), and the use of the radiation condition on Σ , the impedance boundary conditions (Equations (4a;4b)) on S_1 with $Z_s=0$ over S_2 , and the use of the boundary condition in Equation (16) yields:

$$\iint_{S_1} \vec{H}_0 \cdot [Z_s \hat{n} \times \hat{n} \times \vec{H}_b^e] ds = - \iiint_V \vec{H}_b^e \cdot \vec{M}_T dv - \iiint_V \vec{E}_0 \cdot \vec{J} dv \quad ; \quad \text{if } \vec{F} = \vec{J}, \quad (19)$$

and

$$\iint_{S_1} \vec{H}_0 \cdot [Z_s \hat{n} \times \hat{n} \times \vec{H}_b^m] ds = - \iiint_V \vec{H}_b^m \cdot \vec{M}_T dv + \iiint_V \vec{H}_0 \cdot \vec{M} dv \quad ; \quad \text{if } \vec{F} = \vec{M}. \quad (20)$$

\bar{F} is as defined previously in Equation (10b), and $j=1$, $m=1$ for convenience. Also, \bar{M}_T is chosen to be a unit amplitude test source.

$$\bar{M}_T = \hat{T} \delta(|\bar{R}-\bar{R}_P|). \quad (21)$$

Thus, Equations (19) and (20) respectively become

$$\iint_{S_1} \bar{H}_0(\tilde{Q}|P') \cdot [Z_s(\tilde{Q}) \hat{n} \times \hat{n} \times \bar{H}_b^e(\tilde{Q}|P)] ds = - \bar{H}_b^e(P'|P) \cdot \hat{T} - \bar{E}_0(P|P') \cdot \hat{u} ;$$

if $\bar{F}=\bar{J}$, (22)

and

$$\iint_{S_1} \bar{H}_0(\tilde{Q}|P') \cdot [Z_s(\tilde{Q}) \hat{n} \times \hat{n} \times \bar{H}_b^m(\tilde{Q}|P)] ds = - \bar{H}_b^m(P'|P) \cdot \hat{T} + \bar{H}_0(P|P') \cdot \hat{v} ;$$

if $\bar{F}=\bar{M}$. (23)

In Equations (22) and (23), \tilde{Q} represents a point on S_1 and it is therefore a variable of integration; also the notation for the field quantities in terms of the points \tilde{Q} , P , and P' has the same meaning as before (see Equations (11) and (12)).

One may now specialize Equations (22) and (23) to the 2-D TE_z , and TM_z scattering problems of interest by assuming no variation in the z -direction. In the TE_z case, $\bar{F}=\bar{M}$ with $\hat{v}=\hat{z}$; and in the TM_z case, $\bar{F}=\bar{J}$ with $\hat{u}=\hat{z}$. Furthermore, the test source \bar{M}_T in the unperturbed problem is chosen to be $\bar{M}_T=\hat{z}\delta(|\bar{\rho}-\bar{\rho}_P|)$ with $\hat{T}=\hat{z}$ in the TE_z case, thereby constituting a unit amplitude magnetic line source at P' ; on the other hand, \bar{M}_T is chosen to be a magnetic line dipole $\bar{M}_T=\hat{T}\delta(|\bar{\rho}-\bar{\rho}_P|)$ at P' such that $\hat{T}=\hat{\tau}$ (a unit tangent vector to the 2-D boundary S illustrated in Figure 4) as the point P' moves to the point Q' on the boundary S . In fact, the required integral equations result when P' moves to Q' on S in Equations (22) and (23); thus,

$$\int_{S_1} \bar{H}_{0z}(\tilde{Q}|Q') \cdot [Z_s(\tilde{Q}) \hat{n} \times \hat{n} \times \bar{H}_b^m(\tilde{Q}|P)] d\ell = - \bar{H}_b^m(Q'|P) \cdot \hat{z} + \bar{H}_{0z}(P|Q') \cdot \hat{z} ;$$

for $\bar{F}=\bar{M}$, or TE_z case, (24)

and

$$\int_{S_1} \bar{H}_{0\tau}(\tilde{Q}|Q') \cdot [Z_s(\tilde{Q}) \hat{n} \times \hat{n} \times \bar{H}_b^e(\tilde{Q})|P] d\ell = - \bar{H}_b^e(Q'|P) \cdot \hat{\tau} \cdot \bar{E}_{0\tau}(P|Q') \cdot \hat{z};$$

for $\bar{F}=\bar{J}$, or TM_z case. (25)

In order to distinguish between the fields \bar{E}_0, \bar{H}_0 due to $\bar{M}_T = \hat{z}\delta(|\bar{\rho}-\bar{\rho}_Q|)$ for the TE_z case, or $\bar{M}_T = \hat{\tau}\delta(|\bar{\rho}-\bar{\rho}_Q|)$ for the TM_z case, one defines $\bar{E}_{0z}, \bar{H}_{0z}$ as being produced by $\bar{M}_T = \hat{z}\delta(|\bar{\rho}-\bar{\rho}_Q|)$ for the TE_z case; and likewise, one defines $\bar{E}_{0\tau}, \bar{H}_{0\tau}$ as being produced by $\bar{M}_T = \hat{\tau}\delta(|\bar{\rho}-\bar{\rho}_Q|)$ for the TM_z case, as indicated in Equations (24) and (25). It is noted that $ds=d\ell dz$ where $d\ell$ is an incremental arc length along the boundary curve S_1 for the 2-D case, and the integral over dz is suppressed in the 2-D case. In a given coordinate system, the direction of integration along $d\ell$ is chosen to increase in the positive sense such that $ds=d\ell dz > 0$ with dz defined as being in the increasing z -direction.

To be specific, let $d\bar{x} = \hat{\tau}|d\bar{x}|$ so that $\hat{\tau}$ may now represent the increasing coordinate direction for $d\bar{x}$. The latter aspect will be clarified further in the specific applications to planar and cylindrical configurations of Figures 1 and 2. Since \bar{M}_T and \bar{M} are both \hat{z} -directed in the TE_z case, the fields \bar{H}_{0z} and \bar{H}_b^m are also entirely \hat{z} -directed in Equation (24). On the other hand, \bar{M}_T is $\hat{\tau}$ -directed, and \bar{J} is \hat{z} -directed in the TM_z case; thus, $\bar{E}_{0\tau}$ is entirely \hat{z} -directed. Furthermore, it may be shown by applying the reciprocity theorem to the pair of sources \bar{M}_T and \bar{F} in which both \bar{M}_T and \bar{F} now radiate in the presence of the unperturbed, or the perfectly conducting surface S (corresponding to Figure 4(b)) that the field $\bar{H}_{0z}(P|Q')$ in Equation (24), and the field $\bar{E}_{0\tau}(P|Q')$ in Equation (25) are related to the fields $\bar{H}_{ob}^m(Q'|P)$ and $\bar{H}_{ob}^e(Q'|P)$ as follows:

$$\bar{H}_{0z}(P|Q') \cdot \hat{z} = \bar{H}_{ob}^m(Q'|P) \cdot \hat{z}, \quad (26)$$

and

$$\bar{E}_{0\tau}(P|Q') \cdot \hat{z} = - \bar{H}_{ob}^e(Q'|P) \cdot \hat{\tau}. \quad (27)$$

The field $\bar{H}_{ob}^m(Q'|P)$ is generated by $\bar{F}=\bar{M}=\hat{z}\delta(|\bar{\rho}-\bar{\rho}_P|)$ at P in the presence of the unperturbed surface S (Figure 4(b)) for the TE_z case, and it is entirely \hat{z} -directed; whereas, $\bar{H}_{ob}^e(Q'|P)$ is generated by $\bar{F}=\bar{J}=\hat{z}\delta(|\bar{\rho}-\bar{\rho}_P|)$ at P in the presence of the unperturbed surface S (Figure 4(b)) for the TM_z case. The results in Equations (26) and (27) are similar to those in Equations (13) and (14), respectively; in fact, they may be derived in a manner identical to that employed to arrive at Equations

(11) and (12) (or (13) and (14)). Employing Equations (26) and (27) into Equations (24) and (25), respectively together with $\hat{n} \times \hat{n} \cdot \hat{z} = -\hat{z}$, and $\hat{n} \times \hat{n} \cdot \hat{\tau} = -\hat{\tau}$, one obtains the final form of the integral equations as

$$- \int_{S_1} H_{oz}(\tilde{Q}|Q') Z_s(\tilde{Q}) H_b^m(\tilde{Q}|P) d\tilde{z} = -H_b^m(Q'|P) + H_{ob}^m(Q'|P),$$

for TE_z case with \tilde{Q}, Q' on S_1 , (28)

and

$$- \int_{S_1} H_{ot}(\tilde{Q}|Q') Z_s(\tilde{Q}) H_b^e(\tilde{Q}|P) d\tilde{z} = -H_b^e(Q'|P) + H_{ob}^e(Q'|P),$$

for TM_z case with \tilde{Q}, Q' on S_1 , (29)

where the following definitions have been used in Equations (28) and (29).

$$\bar{H}_{oz} \equiv \hat{z} H_{oz} ; \quad \bar{H}_{ob}^m \equiv \hat{z} H_{ob}^m ; \quad \bar{H}_b^m \equiv \hat{z} H_b^m, \quad (30a; 30b; 30c)$$

and

$$\bar{H}_{ot} \cdot \hat{\tau} \equiv H_{ot} ; \quad \bar{H}_{ob}^e \cdot \hat{\tau} \equiv H_{ob}^e ; \quad \bar{H}_b^e \cdot \hat{\tau} \equiv H_b^e . \quad (31a; 31b; 31c)$$

The above integral equations in Equations (28) and (29) are the Fredholm integral equations of the second kind; hence, they could be solved via an iterative procedure. In particular, the kernels in the above integral equations correspond to the terms $H_{oz}(\tilde{Q}|Q')$ and $H_{ot}(\tilde{Q}|Q')$ in Equations (28) and (29), respectively. $H_{oz}(\tilde{Q}|Q')$ represents the \hat{z} -directed magnetic field at \tilde{Q} on the unperturbed surface which is produced by a magnetic line source $\hat{z}\delta(|\vec{\rho}-\vec{\rho}_{Q'}|)$ at the point Q' on the same surface. Likewise, $H_{ot}(\tilde{Q}|Q')$ is the $\hat{\tau}$ -directed magnetic field at \tilde{Q} on the unperturbed surface due to a magnetic line dipole $\hat{\tau}\delta(|\vec{\rho}-\vec{\rho}_{Q'}|)$ at Q' on the same surface. Thus, the kernel is related to the 2-D surface Green's function for the unperturbed boundary. The source term $H_{ob}^m(Q'|P)$ in Equation (28) represents the \hat{z} -directed magnetic field intensity induced at Q' on the unperturbed boundary S due to a unit amplitude magnetic line source $\hat{z}\delta(|\vec{\rho}-\vec{\rho}_P|)$ at P exterior to S . Similarly, the source term $H_{ob}^e(Q'|P)$ in Equation (29) is the $\hat{\tau}$ -directed magnetic field intensity induced at Q' on the unperturbed boundary S due to a unit amplitude electric line source $\hat{\tau}\delta(|\vec{\rho}-\vec{\rho}_P|)$ at P exterior to S . Clearly, in the absence of the perturbation, i.e., when $Z_s=0$, the LHS of Equations (28) and (29) reduce identically to zero so that

$$\left. \begin{aligned} &H_b^m(Q'|P) = H_{ob}^m(Q'|P) \\ \text{and} \quad &H_b^e(Q'|P) = H_{ob}^e(Q'|P) \end{aligned} \right\} \quad \text{if } Z_s = 0,$$

as would be expected. The integral equations (28) and (29) could also have been derived via an application of the compensation theorem for electromagnetic fields [2]. Due to the nature of these equations, they will be referred to in this report as perturbation type integral equations.

The quantities $H_{oz}(\hat{Q}|Q')$ and $H_{ob}^m(Q'|P)$ in Equation (28), and likewise, $H_{ot}(\hat{Q}|Q')$ and $H_{ob}^e(Q'|P)$ in Equation (29) are assumed known. These field quantities are known exactly for the case of planar, and circularly shaped perfectly-conducting boundary S which are considered in this report. In the present analysis, the far zone approximations to $H_{ob}^m(Q'|P)$ and $H_{ob}^e(Q'|P)$ will be employed; furthermore, since the exact eigenfunction series in terms of the radial propagation representation for the fields pertaining to the perfectly-conducting circular cylinder geometry are poorly convergent for large cylinders, the GTD representation for these fields is employed instead. Also, the GTD representation is applicable to perfectly-conducting convex cylinders of non-constant (or variable) curvature thereby making it more useful for the present application. The TE_z and the TM_z cases corresponding to the antenna problems of Figures 1 and 2 are next solved in terms of their respective scattering problems.

The TE_z Problem

A. Planar boundary case: The scattering problem from which one constructs the solution to the problem of the radiation from an axial slot in the planar boundary of Figure 1 is analyzed in this section. The geometry of this TE_z scattering problem, and it's associated "unperturbed" problem corresponding to Figures 4(a) and 4(b) are indicated in Figures 5(a) and 5(b), respectively. The source $\vec{F} = \vec{M} = \hat{z}\delta(|\vec{p} - \vec{p}_p|)$ for the TE_z scattering problem is shown in Figure 5(a), and it is in the far zone of the impedance patch so that the fields due to \vec{M} at Q' (at $y=0$; $|x| < L/2$) are locally plane. On the other hand, the test source $\vec{M}_T = \hat{z}\delta(|\vec{p} - \vec{p}_{Q'}|)$ is at Q' on the unperturbed, or perfectly-conducting boundary as illustrated in Figure 5(b). The \hat{t} -direction indicated in Figures 4(a) and 4(b) is taken to be along \hat{x} in Figures 5(a) and 5(b), respectively (as this corresponds to the increasing \hat{x} -coordinate direction). Thus, Equation (28) becomes in this case, the following.

$$H_{ob}^m(x_{Q'}|P) = \int_{-L/2}^{L/2} dx [\delta(x - x_{Q'}) - Z_s(x) H_{oz}(x|x_{Q'})] H_b^m(x|P); |x, \text{ and } x_{Q'}| < L/2 \quad (32)$$

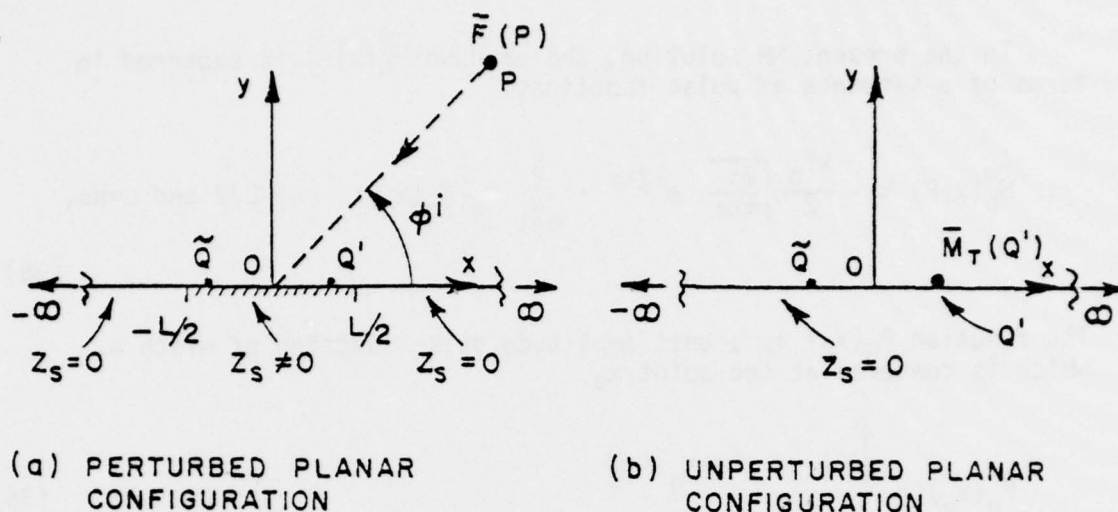


Figure 5. The scattering geometry corresponding to the planar perfectly-conducting surface with a surface impedance patch, and its corresponding unperturbed problem.

in which the coordinates of Q' are $(x=x_{Q'}; y=0)$, and the coordinates of Q are $(x=x; y=0)$.

The field $H_{oz}(x|x_{Q'})$ at a point Q on the unperturbed (perfectly-conducting) surface $y=0$ due to \bar{M}_T at Q' also on the same surface is easily shown to be

$$H_{oz}(x|x_{Q'}) = -\frac{kY_0}{2} H_0^{(2)}(k|x-x_{Q'}|) = H_{oz}(x_{Q'}|x) \quad (33)$$

where Y_0 is the free space admittance, $H_0^{(2)}$ is the cylindrical Hankel function of order zero, and k is the free space wavenumber. Also, $H_{ob}^m(x_{Q'}|P)$ which is the field induced at Q' on the unperturbed surface ($y=0$) due to the source \bar{M} at P external to S is given by

$$H_{ob}^m(x_{Q'}|P) \sim -\frac{kY_0}{2} \cdot \left[\frac{2j}{\sqrt{\pi k\rho}} e^{-jk\rho} \right] \cdot e^{jkx_{Q'} \cos \phi^i}, \quad (34)$$

for the case when the source \bar{M} is in the far zone of the impedance patch ($|x| < L/2; y=0$). The angle ϕ^i in Equation (34) is illustrated in Figure 5. Then, Employing Equations (33) and (34) in (32), one may solve for the unknown $H_B^m(x|P)$ via the conventional MM procedure, provided $Z_s(x)$ is assumed to be a known quantity.

In the present MM solution, the unknown $H_b^m(x|P)$ is expanded in terms of a sequence of pulse functions.

$$H_b^m(x|P) \approx -\frac{kY_0}{2} \sqrt{\frac{2j}{\pi k\rho}} e^{-jk\rho} \cdot \sum_{q=1}^N C_q P_q(x_q); \quad |x| < L/2 \text{ and } L=N\Delta, \quad (35)$$

The function $P_q(x_q)$ is a unit amplitude pulse function of width Δ , which is centered at the point x_q .

$$P_q(x_q) = \begin{cases} 1 & ; \quad |x-x_q| < \frac{\Delta}{2} \\ 0 & ; \quad |x-x_q| > \frac{\Delta}{2} \end{cases} \quad (36)$$

C_q represents the unknown complex coefficients in the above expansion for $H_b^m(x|P)$. Let the point Q' (at $y=0$; $x=x_{Q'}$) take on the following values.

$$x_{Q'} = x_p \quad ; \quad p = 1, 2, \dots, N, \quad (37)$$

with the understanding that x_p corresponds to the mid point of the p^{th} pulse $P_p(x_p)$. This corresponds to point matching (or delta function testing) at the mid points of the pulse expansion functions. Defining

$$f_p \equiv e^{jkx_p \cos \phi^i}, \quad (38)$$

and

$$L_{pq} \equiv \delta_{pq} - \text{P.V.} \int_{x_q - \Delta/2}^{x_q + \Delta/2} dx Z_s(x) \left[-\frac{kY_0}{2} H_0^{(2)}(k|x_p - x|) \right];$$

$$\delta_{pq} \equiv \begin{cases} 1, p=q \\ 0, p \neq q \end{cases}, \quad (39)$$

and incorporating the results of Equations (33) - (39) into Equation (32) yields the following matrix equation for C_q .

$$[f_p]_{N \times 1} = [L_{pq}]_{N \times N} [C_q]_{N \times 1} \quad (40)$$

It is noted that the integration in Equation (39) is over the q^{th} pulse region, and P.V. denotes the principal value of the integral. Finally, a numerical inversion of the matrix $[L_{pq}]$ leads to a solution for the unknown C_q .

B. Circular cylinder case: The scattering problem from which one constructs the solution to the problem of the radiation from an axial slot in the circular cylinder geometry of Figure 2 is analyzed in this section. The geometry of this TE_z scattering problem, and it's associated "unperturbed" problem corresponding to Figures 4(a) and 4(b) are indicated in Figures 6(a) and 6(b) respectively. The source

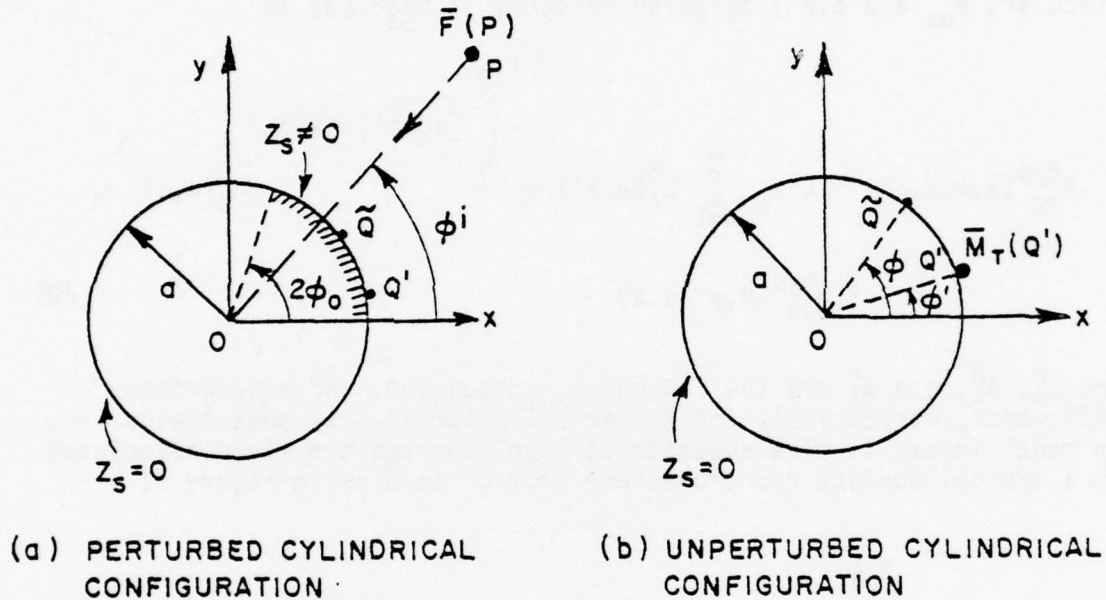


Figure 6. The scattering geometry corresponding to the circular cylinder perfectly-conducting surface with a surface impedance patch, and it's corresponding unperturbed problem.

$\bar{F} = \bar{M} = \hat{z} \delta(|\bar{p} - \bar{p}_p|)$ for this TE_z scattering problem in Figure 6(a), and it is in the far zone of the cylinder; whereas, the test source $\bar{M}_T = \hat{z} \delta(|\bar{p} - \bar{p}_{Q'}|)$ is at Q' on the unperturbed, or perfectly-conducting cylinder as shown in Figure 6(b). In the present case, the \hat{r} -direction in Figures 6(a) and 6(b) is chosen to correspond to the $\hat{\phi}$ direction (as this corresponds to the increasing arc length coordinate $a\phi$). Hence, in this case, Equation (28) becomes

$$H_{ob}^m(a, \phi' | P) = \int_0^{2\phi_0} a \, d\phi [\delta(\phi - \phi') - Z_s(\phi) H_{oz}(a, \phi | a, \phi')] H_b^m(a, \phi | P);$$

$$0 < \phi, \phi' < 2\phi_0, \quad (41)$$

where the coordinates of Q' and \tilde{Q} on the boundary S_1 are (a, ϕ') and (a, ϕ) , respectively; and ϕ_0 is indicated in Figure 6(a).

The quantities, $H_{oz}(a, \phi | a, \phi')$ and $H_{ob}^m(a, \phi' | P)$ are obtained in terms of the GTD results which have been developed elsewhere [3]. In particular, $H_{oz}(a, \phi | a, \phi')$ is given in terms of H_{oz}^{typ} [3] as

$$H_{oz}^{typ}(a, \phi | a, \phi') \sim C \gamma_0 \sum_{\lambda=1}^{\infty} L_{\lambda}^h(a, \phi') e^{-\int_{Q'}^{\tilde{Q}} [\alpha_{\lambda}^h(t') + jk] dt'} A_{\lambda}^h(a, \phi)$$

$$= H_{oz}^{typ}(a, \phi' | a, \phi) \quad (42)$$

where L_{λ}^h , A_{λ}^h , and α_{λ}^h are the launching, attachment, and attenuation coefficients, respectively for Keller's GTD surface ray mode fields with modal index, λ . The superscript "typ" denotes the field associated with a typical surface ray trajectory from Q' to \tilde{Q} as in Figure 7;

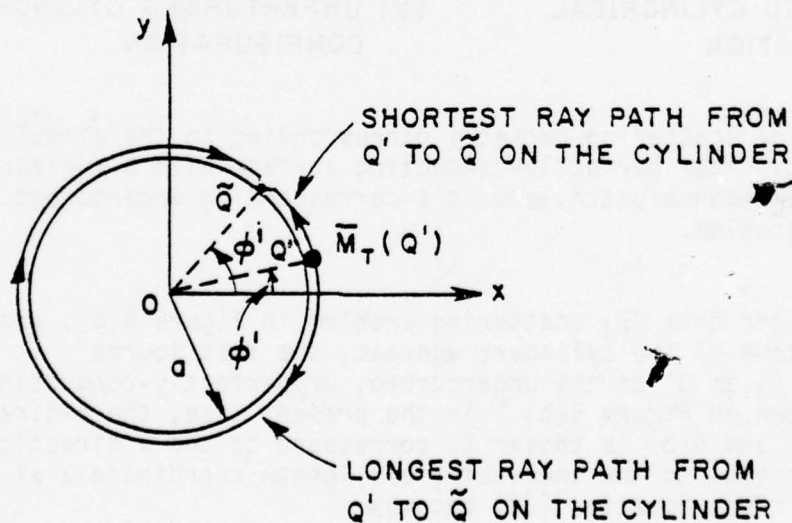


Figure 7. Ray paths around the cylinder for calculating $H_{oz}(a, \phi | a, \phi')$ or $H_{ot}(a, \phi | a, \phi')$.

one notes that there are two such ray paths, and $H_{OZ}(a, \phi | a, \phi')$ is the sum of the fields H_{OZ}^{typ} associated with each of these ray paths.

It is noted that for numerical calculations one generally needs to include only the first couple of modes (corresponding to $\lambda=1$ and $\lambda=2$) to obtain sufficiently accurate results when Q' and Q are not very close to each other. The higher order modes are rapidly attenuated due to the fact that the attenuation constant α_λ^h increases significantly as λ increases. For the circular cylinder case, α_λ^h is a constant for a given radius, "a", and a given mode (or λ). The quantity dt' in Equation (42) is the incremental arc length corresponding to the total arc $Q'Q$. The quantity $H_{OZ}^{typ}(a, \phi' | P)$ is obtained in terms of $H_{OZ}(P | Q')$ which is the field at P due to a magnetic line source at Q' on S, via the relationships in Equation (24) or Equation (26) and Equations (30a;30b); furthermore, $H_{OZ}(P | Q')$ is given in terms of $H_{OZ}^{typ}(P | Q')$ [3] as

$$H_{OZ}^{typ}(P | Q') \sim C Y_0 F \frac{e^{-jks}}{\sqrt{s}}, \quad (43)$$

where

$$F = \sum_{\lambda=1}^{\infty} L_\lambda^h(Q') e^{-\int_{Q'}^Q [\alpha_\lambda^h(t') + jk] dt'} D_\lambda^h(Q); \quad (44a)$$

if P is in the shadow region of Q' ,

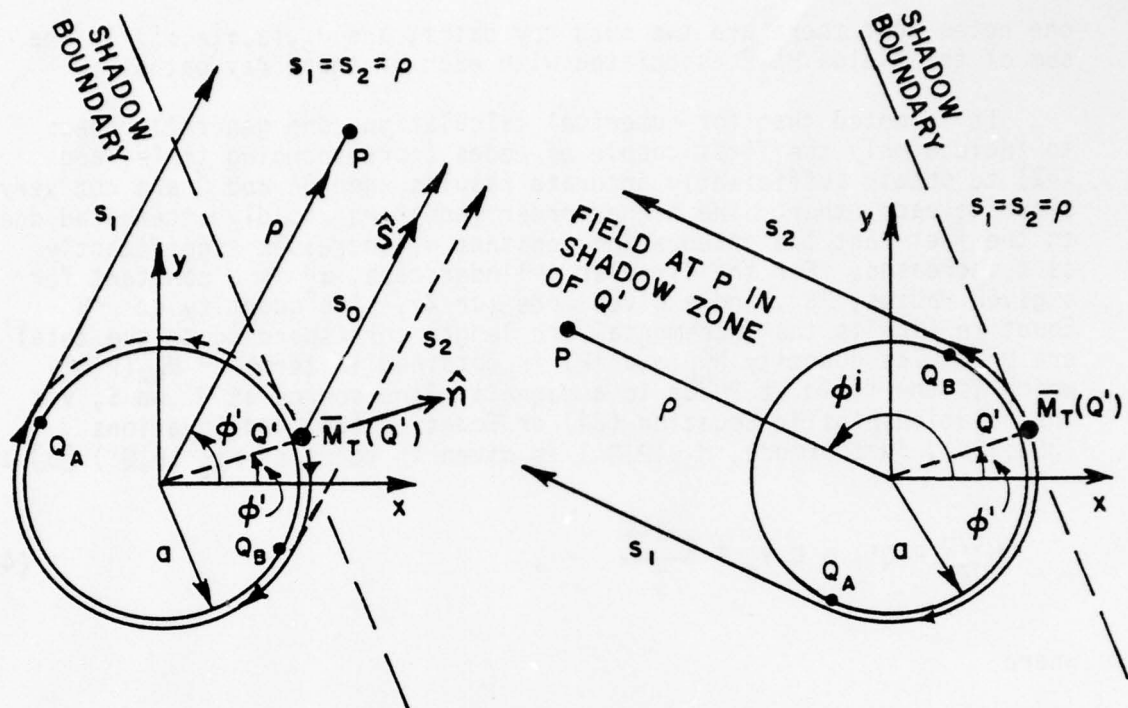
and

$$F = 2 \quad ; \quad \text{if P is in the lit region of } Q'. \quad (44b)$$

$D_\lambda^h(Q)$ in Equation (44a) is the diffraction coefficient for the λ^{th} surface ray mode at the point Q on the boundary S. The constant C appearing in Equations (42) and (43) is given by [3]

$$C = - \frac{k e^{j\pi/4}}{\sqrt{8\pi k}} = - \sqrt{\frac{jk}{8\pi}}. \quad (45)$$

The superscript "typ" in Equation (43) denotes the field associated with a typical ray trajectory from Q' to P as in Figure 8; one notes that in the lit region (see Figure 8a), there are two surface diffracted ray contributions corresponding to ray paths $Q'Q_BQAP$ and $Q'QAQ_BP$, respectively, in addition to the direct ray path $Q'P$. The field of the surface diffracted rays is given by Equation (43) with F as in Equation (44a),



(a) RAYS FROM Q' ARRIVING AT P IN THE LIT ZONE OF Q'

(b) RAYS FROM Q' ARRIVING AT P IN THE SHADOW ZONE OF Q'

Figure 8. Ray paths for calculating $H_{OZ}(P|Q')$ or $E_{OT}(P|Q')$.

whereas, the direct ray field is given by Equation (43) with F as in Equation (44b). The distance s in Equation (43) is s_1 or s_2 corresponding to Q_AP and Q_BP , respectively for the two surface diffracted rays, and $s=s_0=Q'P$ for the direct ray. In the shadow region (see Figure 8b), only the two surface diffracted rays are present. The field $H_{OZ}(P|Q')$ in the lit or shadow regions is thus the sum of the fields $H_{OZ}^{typ}(P|Q')$ of all the rays present in Figures 8a or 8b, respectively. The superscript h on L_λ^h , A_λ^h , D_λ^h and α_λ^h refers to the acoustic hard type surface ray mode which is excited in the TE_z case under consideration.

As Q' approaches \bar{Q} (or vice-versa) in Equation (42), the field point lies in the transition region, and the surface ray mode representation in Equation (42) becomes poorly convergent; thus, it is replaced by a rapidly convergent Fock type integral characterizing the transition region as follows:

$$H_{oz}^{typ}(a, \phi | a, \phi') \sim CY_0 e^{-\int_{Q'}^{\tilde{Q}} jk dt'} \sqrt{\frac{jk}{2\pi}} \left[m(Q') \cdot \frac{\rho_g^{1/6}(\tilde{Q})}{\rho_g^{1/6}(Q')} \right]^{-1} \int_r \frac{w_2(\tau)}{w_2'(\tau)} e^{-j\xi\tau} d\tau \quad (46)$$

where

$$\xi = \int_{Q'}^{\tilde{Q}} \frac{m(t')}{\rho_g(t')} dt' ; \quad m(t') = \left[\frac{k\rho_g(t')}{2} \right]^{1/3}, \quad (47a; 47b)$$

and $\rho_g(t')$ is the radius of curvature of the convex, cylindrical contour S at t' . The quantity $w_2(\tau)$ is the Fock type Airy function, and $w_2'(\tau)$ is its derivative [3].

Following an analysis which is based on some earlier work by H. Bremmer, and by Wait [4], one obtains the following approximation to the Fock type integral of Equation (46).

$$H_{oz}^{typ}(a, \phi | a, \phi') \sim -\frac{kY_0}{2} H_0^{(2)}(k|t|) \left[1 - \frac{\sqrt{\pi j}}{4} \xi^{3/2} + \frac{j7}{60} \xi^3 + \frac{7\sqrt{-\pi j}}{512} \xi^{9/2} + \dots \right]; \quad (48)$$

with $t = \text{arc } \tilde{Q}Q'$.

Clearly Equation (48) converges rapidly for small ξ ; i.e., as $\tilde{Q} \rightarrow Q'$, and it produces the proper singularity at the source (at Q'). Furthermore, the first term in the above expansion represents the result for the planar case as given earlier in Equation (33); and the additional terms in the expansion account for the effects of surface curvature.

The transition region adjacent to the shadow boundary which is associated with the calculation of the field $H_{oz}^{typ}(P|Q')$ in Equation (43) also requires that the GTD ray solution in terms of Equations (44a) and (44b) be modified within this transition region as the field point P moves from the shadow to the lit region (or vice versa) across the shadow boundary. The simple ray descriptions for the fields fail within transition regions across which the different ray representations must change rapidly but smoothly. A uniform result for the transition region which reduces to the proper ray field descriptions in the lit and shadow zones outside the transition region (as required by Equations (44a) and (44b)) is presented in [3]; however, a more convenient representation based on a direct extension of Ivanov's work [5] is presented below.

$$F = g(\xi) e^{-\int_{Q'}^Q j k dt'} \frac{\rho_g^{1/6}(Q)}{\rho_g^{1/6}(Q')} ; \text{ if } P \text{ is in the shadowed part of the transition region (i.e., for } \xi > 0), \quad (49a)$$

with

$$\xi = \int_{Q'}^Q \frac{m(t')}{\rho_g(t')} dt' . \quad (49b)$$

Likewise,

$$F = g(\xi) e^{-j\xi^3/3} ; \text{ if } P \text{ is in the lit part of the transition region (i.e., for } \xi < 0), \quad (50a)$$

with

$$\xi = -m(Q') |\hat{n} \cdot \hat{s}| . \quad (50b)$$

The unit vectors \hat{n} and \hat{s} are indicated in Figure 8a. The acoustic hard Fock function, $g(\xi)$ is tabulated, and it is defined in [3]. It may be verified that Equation (49a) reduces uniformly to Equation (44a) in the deep shadow, whereas Equation (50a) reduces uniformly to Equation (44b) in the deep lit region. Employing the origin as the phase reference for the circular cylinder case under consideration, Equation (43) may be rewritten in the far zone as

$$H_{oz}^{typ}(P|Q') \sim C Y_0 F \frac{e^{-jk\rho}}{\sqrt{\rho}} \cdot e^{j\psi} , \quad (51a)$$

where the phase factor ψ is easily seen to be

$$\psi = \begin{cases} ka \cos[\phi' - \phi^i] & ; \text{ if } P \text{ is in the lit region of } Q' \\ 0 & ; \text{ if } P \text{ is in the shadow region of } Q' . \end{cases} \quad (51b)$$

The angles ϕ' and ϕ^i are indicated in Figures 8a and 8b.

The unknown $H_B^m(a, \phi|P)$ is expanded as before in terms of a set of pulse functions; thus,

$$H_b^m(\tilde{Q}|P) \approx C Y_0 \frac{e^{-jk\rho}}{\sqrt{\rho}} \cdot \sum_{q=1}^N C_q P_q(\phi_q) ; \quad 0 < |\phi| < 2\phi_0$$

and $2\phi_0 = N\Delta$ (52)

where the unit amplitude pulse function $P_q(\phi_q)$ of angular width Δ is centered at the point (a, ϕ_q) .

$$P_q(\phi_q) = \begin{cases} 1 & ; \quad |\phi - \phi_q| < \frac{\Delta}{2} \\ 0 & ; \quad |\phi - \phi_q| > \frac{\Delta}{2} \end{cases} . \quad (53)$$

In order to evaluate the unknown coefficients C_q in the expansion of Equation (52), one employs point matching (or delta function testing) at the center of each pulse; i.e., one lets the point Q' at (a, ϕ') take on the following values,

$$\phi' = \phi_p ; \quad p = 1, 2, \dots, N , \quad (54)$$

with the understanding that (a, ϕ_p) is the center of the p^{th} pulse $P_p(\phi_p)$.

As done before for the planar case, one may incorporate the results of Equations (42) - (54) into Equation (41) to arrive at a matrix equation analogous to that in Equation (40) from which the unknown C_q may be found via a numerical matrix inversion procedure. It is noted that the arc length integrals in Equations (42), (44a), (46), (47a), (49a) and (49b) are trivially integrated in closed form for the circular cylinder case; however, the general forms of these integrals have been presented to indicate that the above method of solution is also applicable to convex cylinders of nonconstant curvature.

The TM_z Problem

A. Planar boundary case: The scattering problem from which one constructs the solution to the problem of the radiation from a circumferential slot in the planar boundary of Figure 1 is analyzed in this section. The geometry of this TM_z scattering problem, and it's associated "unperturbed" problem corresponding to Figures 4a and 4b are indicated in Figures 5a and 5b, respectively. The source \vec{F} is now of the type $\vec{F} = \hat{z}\delta(|\vec{\rho} - \vec{\rho}_p|)$ in the TM_z case; whereas, the test source \vec{M}_T is given by $\vec{M}_T = \hat{x}\delta(|\vec{\rho} - \vec{\rho}_Q|)$ at Q' on the unperturbed (or perfectly-conducting) surface with the $\hat{\tau}$ direction being along \hat{x} in this case. The corresponding integral equation for the TM_z case becomes via Equation (29):

$$H_{ob}^e(x_{Q'}, |P) = \int_{-L/2}^{L/2} dx [\delta(x-x_{Q'}) - Z_s(x) H_{ot}(x|x_{Q'})] H_b^e(x|P);$$

$$|x| < L/2$$

$$|x_{Q'}| < L/2, \quad (55)$$

in which the coordinates of Q' are $(x=x_{Q'}; y=0)$, and the coordinates of Q are $(x=x; y=0)$.

The field $H_{ot}(x|x_{Q'})$ at Q' on the unperturbed surface due to \bar{M}_T at Q also on the same surface is easily shown to be

$$H_{ot}(x|x_{Q'}) = -\frac{kY_0}{2} \frac{H_1^{(2)}(k|x-x_{Q'}|)}{k|x-x_{Q'}|} = H_{ot}(x_{Q'}|x) \quad (56a)$$

in which $H_1^{(2)}$ is the cylindrical Hankel function of order one. It is noted that $H_{ot}(x|x_{Q'})$ is more singular than $H_{oz}(x|x_{Q'})$ of Equation (33) for the TE_z case; consequently, an alternative representation for $H_{ot}(x|x_{Q'})$ which will be employed for $x_{Q'} \rightarrow x$ in the present analysis is

$$H_{ot}(x_{Q'}|x) = -\frac{kY_0}{2} \left[H_0^{(2)}(k|x-x_{Q'}|) + \frac{1}{k^2} \frac{\partial^2}{\partial x_{Q'}^2} H_0^{(2)}(k|x-x_{Q'}|) \right]. \quad (56b)$$

The field $H_{ob}^e(x_{Q'}|P)$ due to \bar{J} which is induced at Q' on the unperturbed surface is given by

$$H_{ob}^e(x_{Q'}|P) \sim -\frac{k}{2} \left[\sqrt{\frac{2j}{\pi k\rho}} e^{-jk\rho} \right] \sin\phi^i e^{jkx_{Q'} \cos\phi^i}, \quad (57)$$

when the source \bar{J} is in the far zone of the surface impedance patch region. The angle, ϕ^i is illustrated in Figure 5. One may incorporate Equations (56b) and (57) into Equation (55) and solve for $H_b^e(x|P)$ via the MM procedure; thus, one may expand $H_b^e(x|P)$ in terms of a sequence of pulse functions as

$$H_b^e(x|P) = -\frac{k}{2} \sqrt{\frac{2j}{\pi k\rho}} e^{-jk\rho} \sum_{q=1}^N C_q P_q(x_q); \quad |x| < L/2, \text{ and } L = N\Delta. \quad (58)$$

The function $P_q(x_q)$ is defined previously in Equation (36); and C_q are the unknown coefficients which are to be determined.

Let

$$g_q(x_p) \equiv \text{P.V.} \int_{x_q - \Delta/2}^{x_q + \Delta/2} dx Z_s(x) H_0^{(2)}(k|x-x_p|) . \quad (59)$$

Also,

$$\left. \frac{\partial^2}{\partial x_{Q'}^2} g_q(x_{Q'}) \right|_{x_{Q'}=x_p} \approx \frac{g_q(x_p^+) - 2g_q(x_p) + g_q(x_p^-)}{h^2} ; \text{ at } x_{Q'}=x_p \quad (60)$$

where

$$h \equiv \lambda \Delta/2 ; \text{ with } \lambda < 1, \quad (61)$$

and

$$x_p^\pm = x_p \pm h \quad (\text{specifically, } x_p \text{ is defined in (63) below}). \quad (62)$$

A finite difference approximation has been employed in Equation (60), and the finite difference width, $2h$ depends on the parameter λ as indicated in Equation (61). The quantity Δ in Equation (61) of course corresponds to the width of the expansion pulse $P_q(x_q)$.

In the present case, the choice of λ is critical, and the value of $\lambda/2$ chosen is approximately 23/60; more will be indicated on this choice of λ for obtaining stable numerical results in Section III. The unknown C_q may be found by solving a set of simultaneous linear equations obtained by allowing the point Q' (at $x=x_{Q'}$, $y=0$) to take on the values

$$x_{Q'} = x_p , \quad p = 1, 2, \dots, N, \quad (63)$$

which corresponds to point matching at the center of the pulses. Defining

$$a_p \equiv \sin \phi^i e^{jkx_p \cos \phi^i} , \quad (64)$$

and

$$N_{pq} \equiv \delta_{pq} + \frac{kY_0}{2} \left[g_q(x_p) + \frac{1}{k^2} \left. \frac{\partial^2}{\partial x_{Q'}^2} g_q(x_{Q'}) \right|_{x_{Q'}=x_p} \right] , \quad (65)$$

one may express the set of equations for C_q compactly in a matrix notation in terms of a_p and N_{pq} as

$$[a_p]_{N \times 1} = [N_{pq}]_{N \times N} [C_q]_{N \times 1} \quad (66)$$

Thus, C_q may be obtained via a numerical matrix inversion of $[N_{pq}]$.

B. Circular cylinder case: The scattering problem from which one constructs the solution to the problem of the radiation from a circumferential slot in the circular cylinder geometry of Figure 2 is analyzed in this section. The geometry of this TM_z scattering problem, and its associated "unperturbed" problem corresponding to Figures 4a and 4b are indicated in Figures 6a and 6b respectively. The source $\vec{F} = \hat{z} \delta(|\vec{p} - \vec{p}_0|)$ for this TM_z scattering problem in Figure 6a, and it is in the far zone of the cylinder; whereas, the test source $\vec{M}_T = \hat{\phi} \delta(|\vec{p} - \vec{p}_0|)$ is at Q' on the unperturbed (or perfectly-conducting) cylinder as shown in Figure 6b. The $\hat{\tau}$ -direction has of course been chosen to correspond to the $\hat{\phi}$ -direction. Thus, the TM_z integral equation for this problem becomes via Equation (29) the following.

$$H_{ob}^e(a, \phi' | P) = \int_0^{2\phi_0} a d\phi [\delta(\phi - \phi') - Z_s(\phi) H_{o\tau}(a, \phi | a, \phi')] H_b^e(a, \phi | P); \quad 0 < \phi, \phi' < 2\phi_0, \quad (67)$$

where the coordinates of Q' and \tilde{Q} on the boundary S_1 are (a, ϕ') and (a, ϕ) , respectively as in the TE_z case (see Equation (41)); and ϕ_0 is as in Figure 6a.

Following the procedure for solving the TE_z cylinder, one begins by incorporating the GTD approximations for $H_{o\tau}(a, \phi | a, \phi')$ and $H_{ob}^e(a, \phi' | P)$. Thus, $H_{o\tau}^{typ}(a, \phi | a, \phi')$ where the superscript "typ" has the same meaning as in Equation (42) for the TE_z case is given by [3]

$$\begin{aligned} H_{o\tau}^{typ}(a, \phi | a, \phi') &= CY_0 \sum_{\ell=1}^{\infty} L_{\ell}^S(a, \phi') e^{-\int_{Q'}^{\tilde{Q}} [\alpha_{\ell}^S(t') + jk] dt'} A_{\ell}^S(a, \phi) \\ &= H_{o\tau}^{typ}(a, \phi' | a, \phi) \end{aligned} \quad (68)$$

L_{ℓ}^S , A_{ℓ}^S and α_{ℓ}^S are now the launching, attachment, and attenuation coefficients for the ℓ th GTD surface ray mode. Again, an inclusion of only the first couple of modes is sufficient for obtaining accurate results when the points Q' and \tilde{Q} are not too close to each other.

$H_{0\tau}(a, \phi | a, \phi')$ is the sum of the fields H_{0z}^{typ} associated with each of the two ray paths illustrated in Figure 7.

The quantity $H_{0b}^e(a, \phi' | P)$ is obtained in terms of $E_{0\tau}(P | Q')$ which is the field at P due to a magnetic line dipole source at Q' on S via the relationships in Equations (25) or (27) and (30a;30b); in particular $E_{0\tau}^{typ}(P | Q')$ is given by [3]:

$$E_{0\tau}^{typ}(P | Q') \sim C G \frac{e^{-jks}}{\sqrt{s}} \quad (69)$$

where the meaning of the superscript "typ" and the distance s is the same as in Equation (43), and where

$$G = \sum_{\lambda=1}^{\infty} L_{\lambda}^S(Q') e^{-\int_{Q'}^Q [\alpha_{\lambda}^S(t') + jk] dt'} D_{\lambda}^S(Q); \quad \text{if P is in the shadow region of } Q', \quad (70a)$$

and

$$G = 2 |\hat{n} \cdot \hat{s}|; \quad \text{if P is in the lit region of } Q'. \quad (70b)$$

The $D_{\lambda}^S(Q)$ in Equation (70a) is the diffraction coefficient of the λ^{th} surface ray mode at Q. The constant C in Equation (69) is given previously in Equation (45), and the superscript s on L_{λ}^S , A_{λ}^S , D_{λ}^S and α_{λ}^S refers to the acoustic soft type surface ray mode which is excited in the TM_z case under consideration. The ray trajectories associated with $E_{0\tau}^{typ}(P | Q')$ in Equation (69) are indicated in Figure 8, and $E_{0\tau}$ is the sum of the fields $E_{0\tau}^{typ}$ which are associated with the rays shown in this figure.

As in the TE_z case, when Q' and \tilde{Q} are sufficiently close, one is within the transition region, and Equation (68) must be replaced by a more rapidly converging Fock type integral as

$$H_{0\tau}^{typ}(a, \phi | a, \phi') \sim -CY_0 e^{-\int_{Q'}^{\tilde{Q}} jk dt'} \sqrt{\frac{jk}{2\pi}} \left[m(Q') \frac{\rho_g^{1/6}(\tilde{Q})}{\rho_g^{1/6}(Q')} \right]^{-3} \int_{\tilde{r}}^{\tau} \frac{w_2'(\tau)}{w_2(\tau)} e^{-j\xi\tau} d\tau \quad (71)$$

where the quantities, ξ , ρ_g , m , w_2 and w_2' appearing above are the same as in Equation (46). An extension of the analysis in [4] to the TM_z case yields the following approximation to Equation (71) as

$$H_{0\tau}^{typ}(a, \phi | a, \phi') \sim -\frac{kY_0}{2} \frac{H_1^{(2)}(k|t|)}{k|t|} \left[1 - \frac{\sqrt{\pi j}}{2} \xi^{3/2} + \frac{j5}{12} \xi^3 + \frac{5}{64} \sqrt{-\pi j} \xi^{9/2} + \dots \right]. \quad (72a)$$

The above approximation is analogous to that in Equation (48) for the TE_z case; and as in Equation (48) it is seen that the first term of the expansion in Equation (72) represents the flat or planar surface result corresponding to Equation (56a), with the additional terms representing the correction to the flat surface result arising from the presence of finite curvature of the cylinder. Following the alternative representation for Equation (56a) given in Equation (56b), one may also rewrite Equation (72a) for the circular cylinder as:

$$H_{0\tau}^{typ}(a, \phi' | a, \phi) \sim -\frac{kY_0}{2} \left[H_0^{(2)}(k|t|) + \frac{1}{(ka)^2} \frac{\partial^2}{\partial \phi'^2} H_0^{(2)}(k|t|) \right] \cdot \left[1 - \frac{\sqrt{\pi j}}{2} \xi^{3/2} + \frac{j5}{12} \xi^3 + \frac{5}{64} \sqrt{-\pi j} \xi^{9/2} + \dots \right] \quad (72b)$$

where $|t| = a|\phi - \phi'|$ in the circular cylinder case. The above could be generalized to arbitrary convex cylinders using the local properties of asymptotic high frequency results. The result in Equation (72b) is useful for large ka and small $|t|$ (i.e., for small ξ).

One must also modify the function G in Equation (69) as the point P moves within the transition region across the shadow boundary as done for the function F in Equations (49) and (50) for the TE_z case. Based on the work in [5], one obtains

$$G = \frac{-j}{m(Q')} \tilde{g}(\xi) e^{-\int_{Q'}^Q jk dt'} \cdot \frac{\rho_g^{1/6}(Q)}{\rho_g^{1/6}(Q')} ; \quad \text{if } P \text{ is in the shadowed part of the transition region (i.e., for } \xi > 0), \quad (73)$$

with ξ as in Equation (49b); and,

$$G = \frac{-j}{m(Q')} \tilde{g}(\xi) e^{-j\xi^3/3} ; \quad \text{if } P \text{ is in the lit part of the transition region (i.e., for } \xi < 0), \quad (74)$$

with ξ as in Equation (50b), respectively. The acoustic soft Fock function, $\tilde{g}(\xi)$ is tabulated, and it is defined in [3].

It may be verified that Equation (73) reduces to Equation (70a) in the deep shadow, whereas Equation (74) reduces to Equation (70b) in the deep lit region thereby providing a uniform approximation to G within the transition region across the shadow boundary. Using the origin as the phase reference, one replaces $\frac{e^{-jks}}{\sqrt{s}}$ in Equation (69) by $\frac{e^{-jk\rho}}{\sqrt{\rho}} e^{j\psi}$ where ψ is defined in Equation (51b).

The unknown $H_b^e(a, \phi | P)$ is then expanded in terms of a set of pulse functions as

$$H_b^e(\tilde{Q} | P) \approx c \frac{e^{-jk\rho}}{\sqrt{\rho}} \sum_{q=1}^{\infty} C_q P_q(\phi_q) \quad (75)$$

analogous to that in Equation (52) for the TE_z case. For $|t|$ or $\xi \rightarrow 0$, the approximation in Equation (72b) is employed instead of Equation (72a), and the $\frac{\partial^2}{\partial \phi^2}$ derivative is approximated via the finite difference scheme similar to that indicated in Equation (60) for the planar TM_z case.

Then employing point matching (or impulse testing) at $\phi' = \phi_p$, $p=1, 2, \dots, N$ as in the TE_z case, one arrives at a matrix equation of the form

$$[a_p]_{N \times 1} = [N_{pq}]_{N \times N} [C_q]_{N \times 1} \quad (76)$$

analogous to the planar TM_z case from which the unknown C_q may be found by a numerical inversion of $[N_{pq}]$. The explicit forms of a_p and N_{pq} are not presented for the sake of brevity, but they are easily found from the results for H_{0T} and E_{0T} presented above. The finite difference width is chosen to be the same as that determined for the planar TM_z case.

III. NUMERICAL RESULTS AND DISCUSSION

Having obtained the solutions to the surface field induced in the problem of scattering of electromagnetic waves by planar and cylindrical perfectly-conducting surfaces which are covered by a surface impedance patch of finite extent, one may then directly calculate the radiation pattern of a thin slot placed within the surface impedance region of these configurations via the reciprocity principle as indicated in the previous section.

Basically, the radiation pattern calculation amounts to finding the amplitude C_q of the q^{th} expansion pulse representing the value of the induced surface magnetic field in the scattering problems such that this q^{th} pulse is centered at the slot location in the corresponding antenna problem. The radiation pattern of this slot in the ϕ^1 direction (see Figures 5 and 6) is then obtained by calculating the value of C_q due to the source \bar{F} at (ρ, ϕ^1) in the scattering problem. In the present calculations, C_q is calculated for every two degree increment in ϕ^1 .

The moment method solution of the perturbation integral equations is carried out using pulse expansion functions, and impulse (or delta) testing functions; this choice of expansion and test functions has been primarily selected for simplicity. As mentioned in the previous section, the TM_z solutions presented some numerical difficulties due to the more singular nature of the kernel.

While pulse expansion functions and piecewise sinusoidal test functions were initially employed to circumvent this difficulty, it turned out that the numerical results were sensitive to the width of the test function in this case. On the other hand, the finite difference approximation employed together with pulse expansion and impulse test functions led to results which were sensitive to the choice of the finite difference width. Results sensitive to the width of test functions, and also to finite difference intervals have been encountered elsewhere in the MM solutions to wire antenna problems [6,7].

The advantages gained by employing the perturbation type integral equation which requires the unknown to be solved only over the surface impedance patch may thus appear to be negated for the TM_z case due to the occurrence of a more singular kernel than that which is present in the conventional electric field integral equation (EFIE).

The EFIE is a special case of the reaction integral equation [8]. However, it is shown that once the proper finite difference width is chosen (this width is then the same for all the TM_z cases considered herein), the results for the TM_z case are indeed stable and can be simply computed. In the present analysis, the finite difference width was varied until it yielded a value for a certain parameter in the problem which agreed closely with that obtained via an accurate, independent procedure. One recalls that the finite difference scheme is required in the TM_z case to approximate the second derivative in the kernel of Equation (56b) or Equation (72b).

In actual numerical computations, the representations for the kernels in Equations (56b) and (72b) corresponding to the planar and cylindrical cases were employed only for computing the elements N_{11} , N_{12} and N_{13} (note: $N_{11} = N_{22} = N_{33} = \dots = N_{pp}$) in Equations (66) and (76), respectively; whereas, the representations in Equations (56a) and (72a) were employed for calculating all other N_{pq} elements with $q \geq p+3$. The N_{pq} for $q < p$ are then obtained from N_{pq} for $q > p$ via symmetry since $N_{pq} = N_{qp}$.

The results of the radiation pattern calculation of slots in the planar and cylindrical configurations of Figures 1 and 2 are indicated in Figures 9-22 for the axial slot (or TE_z) case, whereas those for the circumferential slot (or TM_z) case are indicated in Figures 23-29, respectively.

These MM-GTD results are compared with numerical results obtained by other independent methods which are based on either the complete GTD approach [11] or the complete MM solution of the conventional reaction integral equations for the same problems. Also, an exact eigenfunction series expansion is available for calculating the radiation from slots in circular cylinders which are completely covered with an impedance surface. Such an expansion has been computed for a few TE_z cases to provide a comparison with the corresponding MM-GTD results as indicated in Figures 12 and 13. Indeed, the agreement between the results based on the present MM-GTD method and by other independent methods is in general quite good. Unless otherwise specified, the patterns are normalized to 0 dB at their peak values. Figure 17 indicates the effect of changing the value of the surface impedance patch on a cylinder from an inductive to a capacitive type reactance for the axial slot (or the TE_z) case. It is noted that a capacitive reactance will not support an Elliot type mode in the TE_z problem, and therefore, the gain near the horizon would be reduced in this case.

Radiation pattern calculations via the MM-GTD method are included to illustrate the effects of changing the size of the surface impedance patch, changing the value of the surface impedance, and also changing the size of the circular cylinder. In general, it is seen that increasing the size of the impedance patch increases the number of pattern ripples in the lit region, i.e., in the region of space where the slot is directly visible; whereas, increasing the size of the cylinder tends to decrease the level of the radiation pattern in the deep shadow region of the slot. Over the range of impedance values considered in the present calculations one notes that increasing the magnitude of the surface impedance increases the size of pattern ripple in the lit region for the TE_z case, whereas it does the opposite for the TM_z case. A means to reduce the level of the pattern ripple in the lit region is to appropriately taper the surface impedance as indicated in Figure 16.

In conclusion, a perturbation type integral equation has been employed for solving the antenna problems illustrated in Figures 1 and 2 via a combination of MM and GTD approaches. This procedure requires the unknown to be evaluated via the MM procedure only over the surface impedance patch region, hence it is different from the MM solution of conventional integral equations (for the same problem) which employ the free space Green's function, as the latter requires the unknown to be evaluated not only over the surface impedance patch region, but also over the rest of the perfectly conducting region. The systematic use of the GTD provides simplifications in the MM calculations, and it allows one to treat convex cylinders with variable curvature without much difficulty. Thus, the present approach can treat electrically large perfectly-conducting cylinders (with impedance patches) far more efficiently than by the use of the conventional integral equations. Furthermore, the GTD approximations incorporated in the kernel and source terms of the perturbation integral equations become increasingly accurate as the frequency increases, and in general these GTD approximations are quite accurate even for ka as small as 6.

Further work needs to be done to arrive at a more satisfactory approach for obtaining a proper choice of the finite difference width in the circumferential slot (or TM_z) case. For example, one might investigate how well the appropriate boundary conditions are met on the perfectly-conducting portion as a function of the finite difference width, or investigate some other simpler criteria determining this finite difference width.

With the present solutions one could now begin to investigate the CP characteristics of crossed slots in the surface impedance loaded circular cylinders as a function of the different parameters involved. In addition, it would be of interest to include loss in the surface impedance to study how that would affect the pattern shape and CP characteristics of crossed slots in cylinders. The extension of this analysis to include airplane wing effects in the roll plane can be carried out via GTD in which the fields incident on the wings may be calculated via the present MM-GTD approach, while the reflections from the wing surface and the diffractions from the wing tips due to the fields incident on the wings may be easily and simply calculated via the ray reflection and diffraction coefficients as in [10].

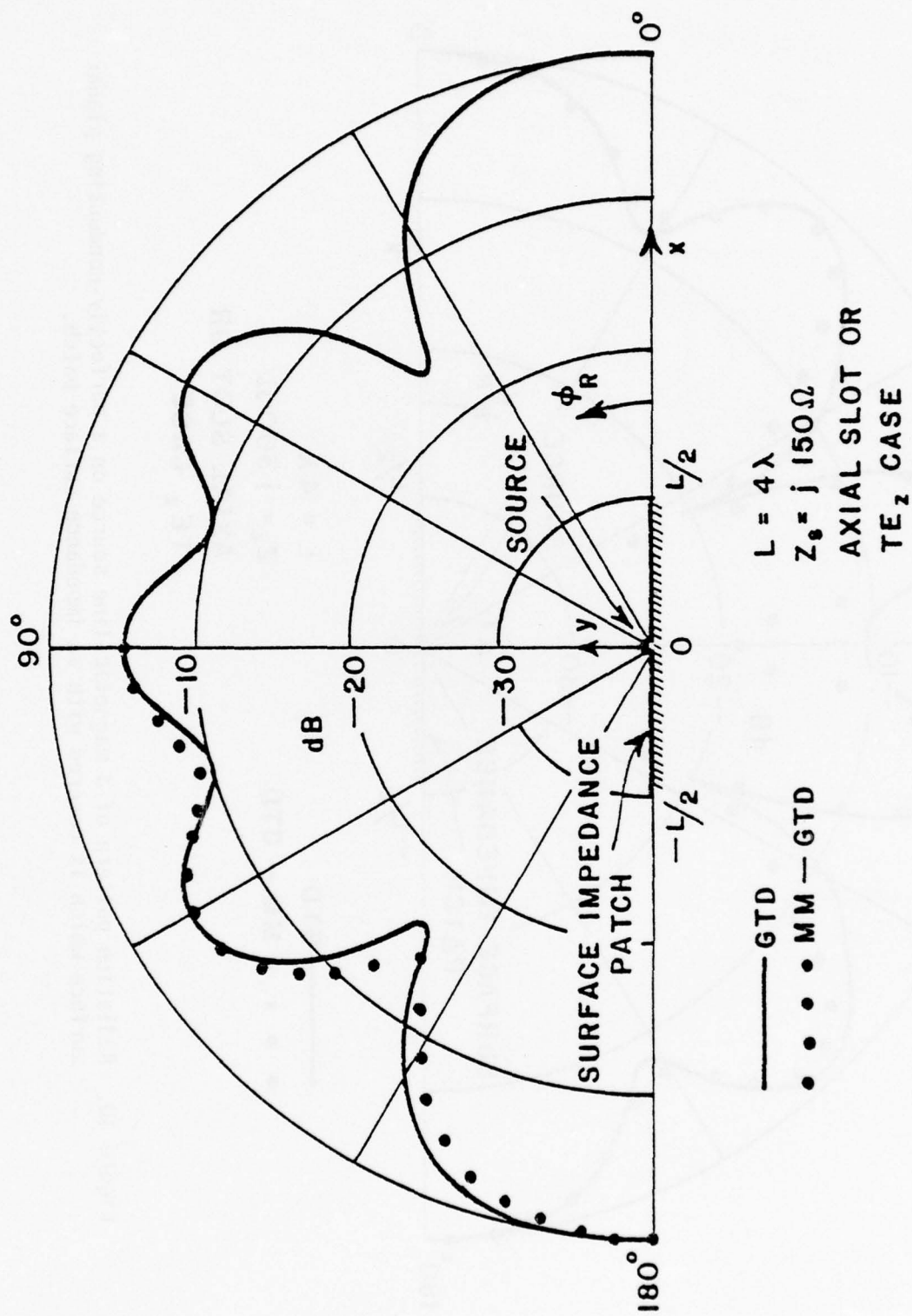


Figure 9. Radiation pattern of a magnetic line source on a perfectly-conducting planar surface which is covered with an impedance surface patch.

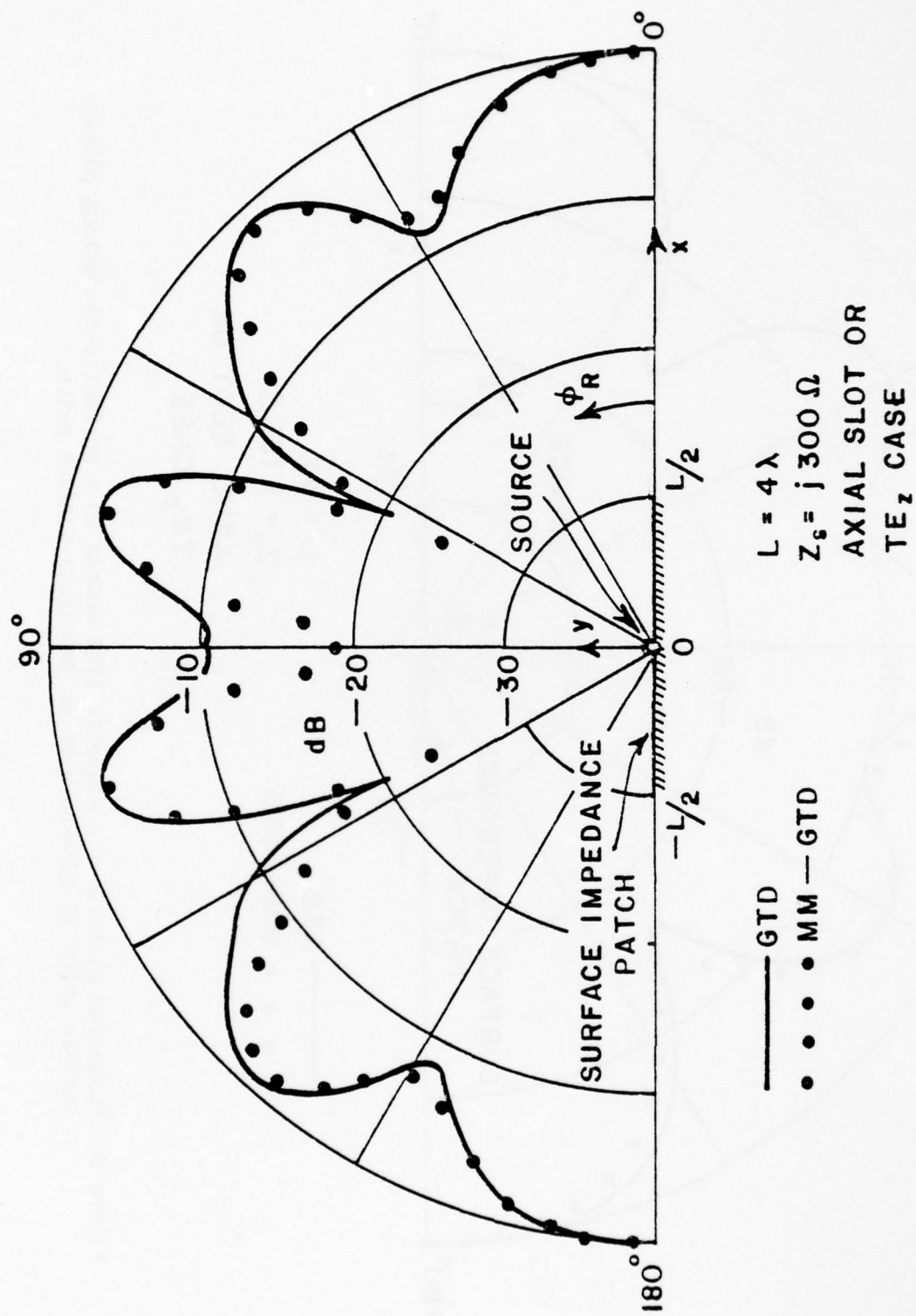


Figure 10. Radiation pattern of a magnetic line source on a perfectly-conducting planar surface which is covered with an impedance surface patch.

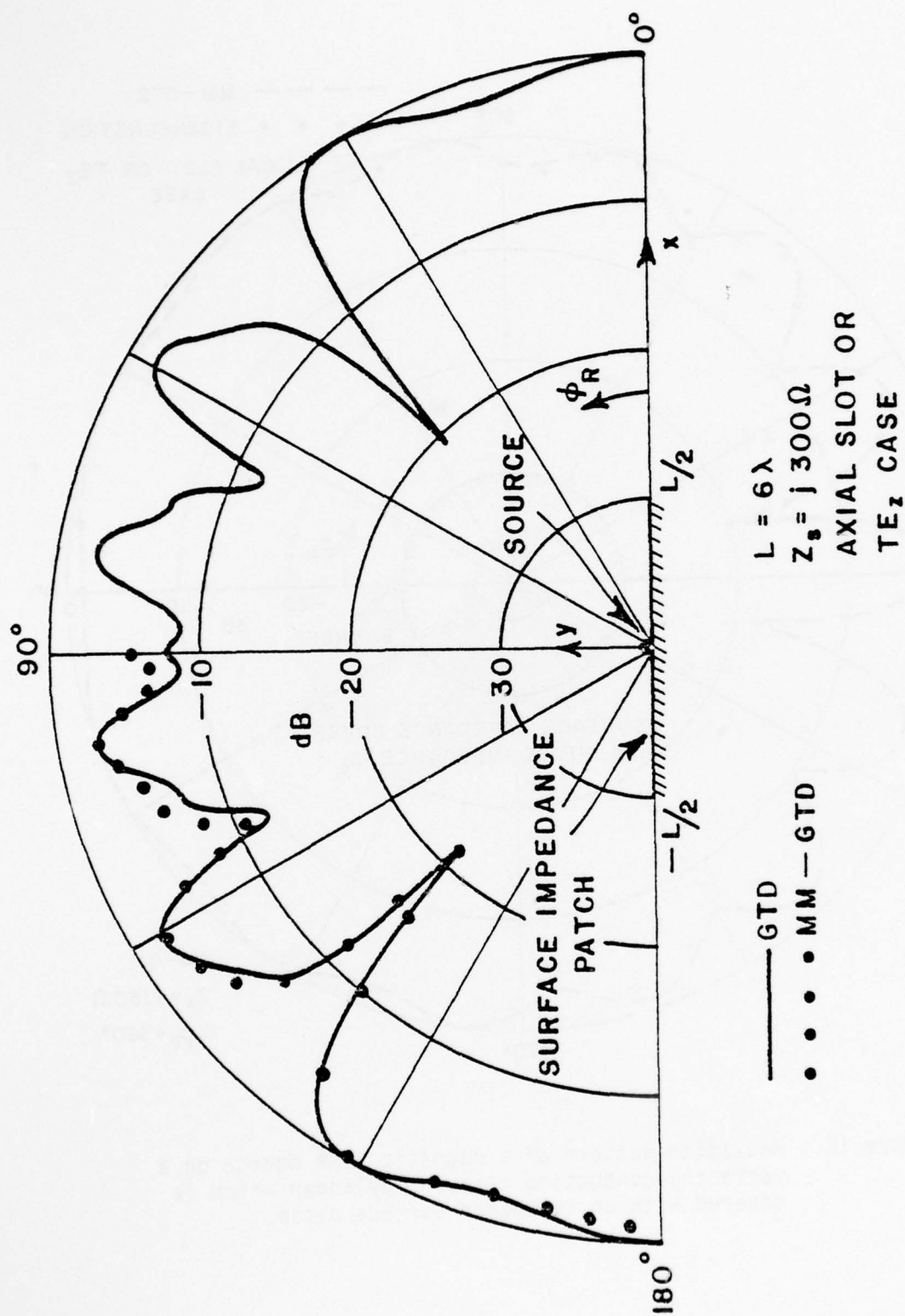


Figure 11. Radiation pattern of a magnetic line source on a perfectly-conducting planar surface which is covered with an impedance surface patch.

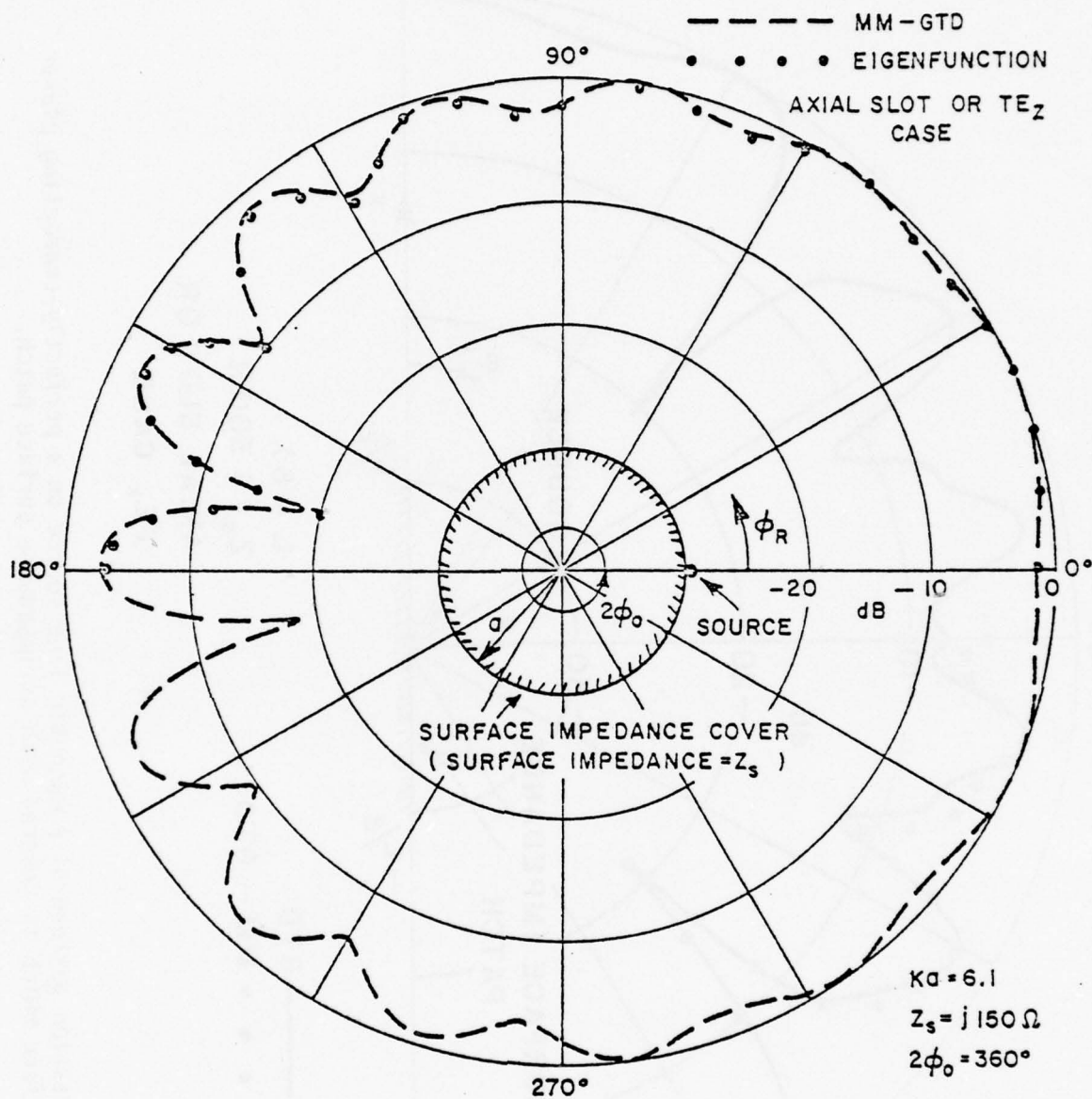


Figure 12. Radiation pattern of a magnetic line source on a perfectly-conducting circular cylinder which is covered with an impedance surface patch.

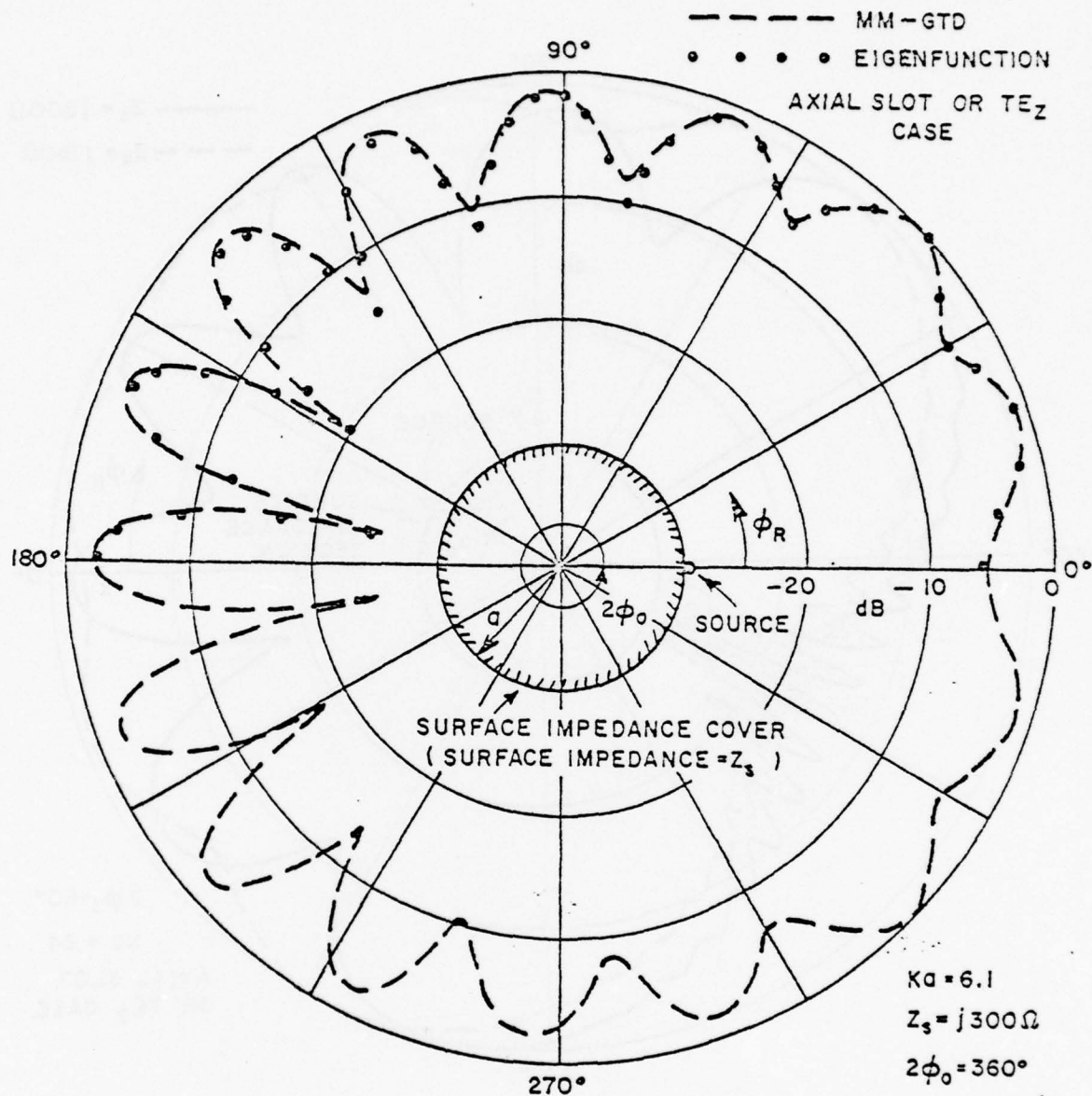


Figure 13. Radiation pattern of a magnetic line source on a perfectly-conducting circular cylinder which is covered with an impedance surface patch.

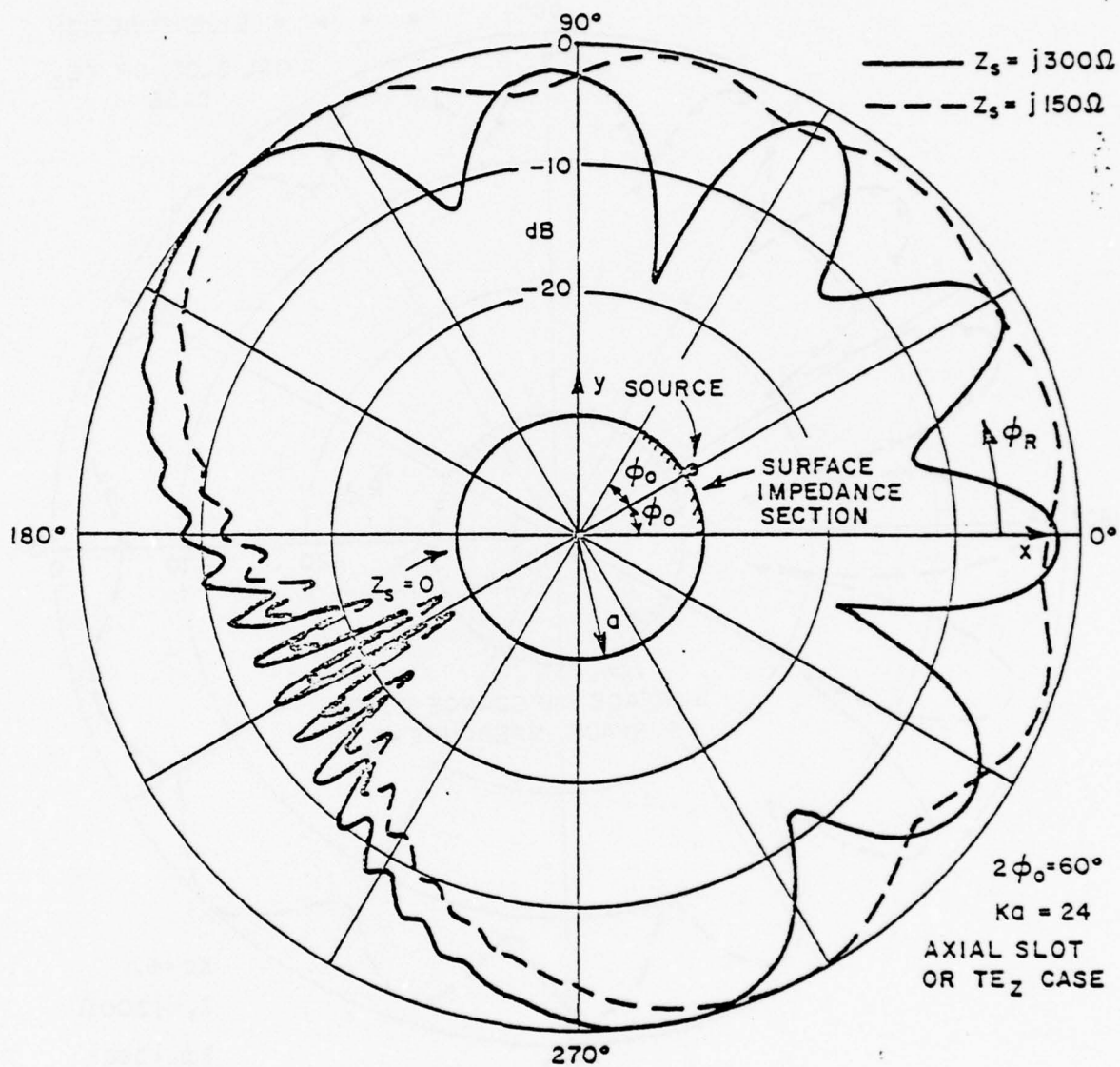


Figure 14. Radiation pattern of a magnetic line source on a perfectly-conducting circular cylinder which is covered with an impedance surface patch.

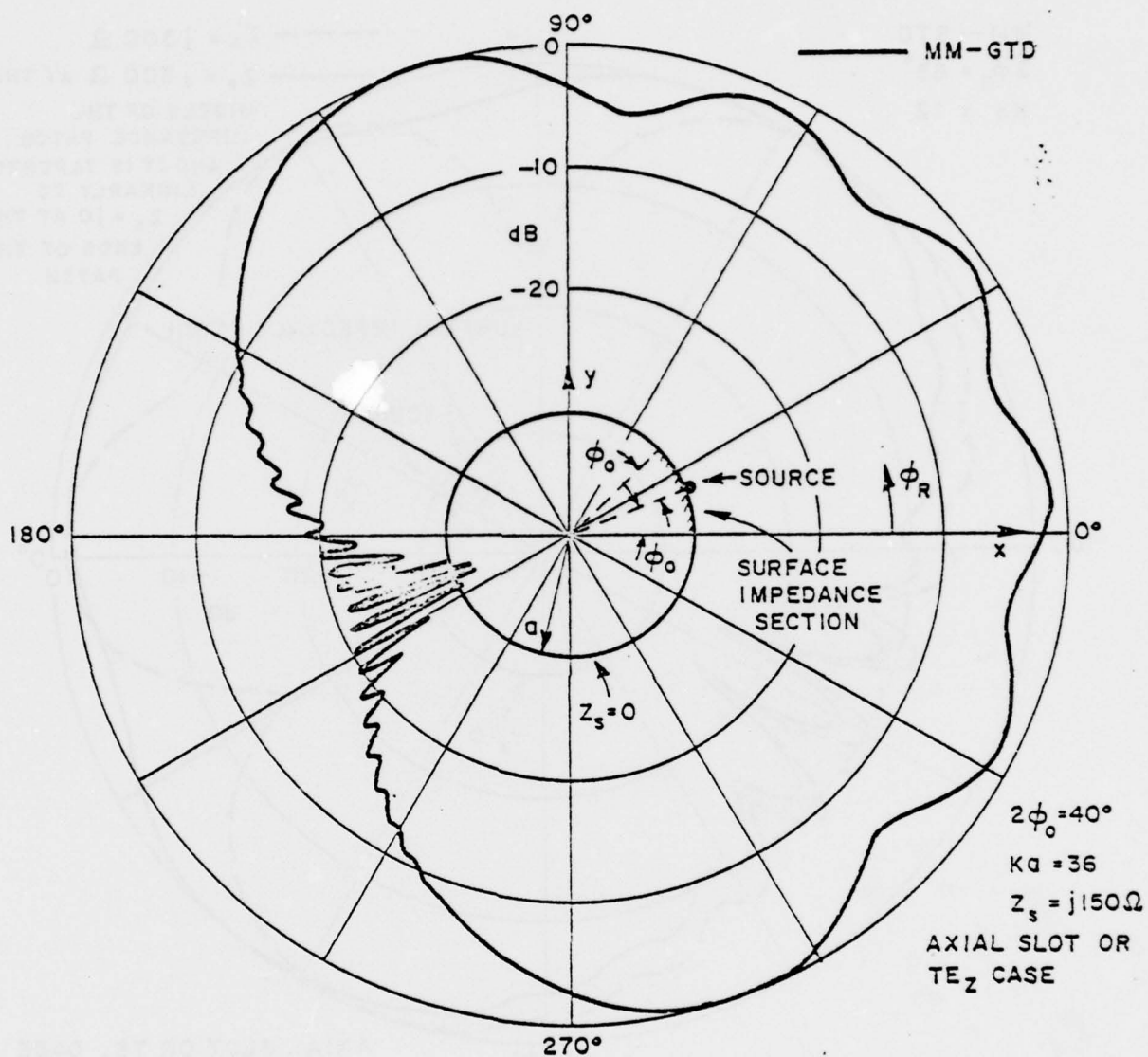


Figure 15. Radiation pattern of a magnetic line source on a perfectly-conducting circular cylinder which is covered with an impedance surface patch.

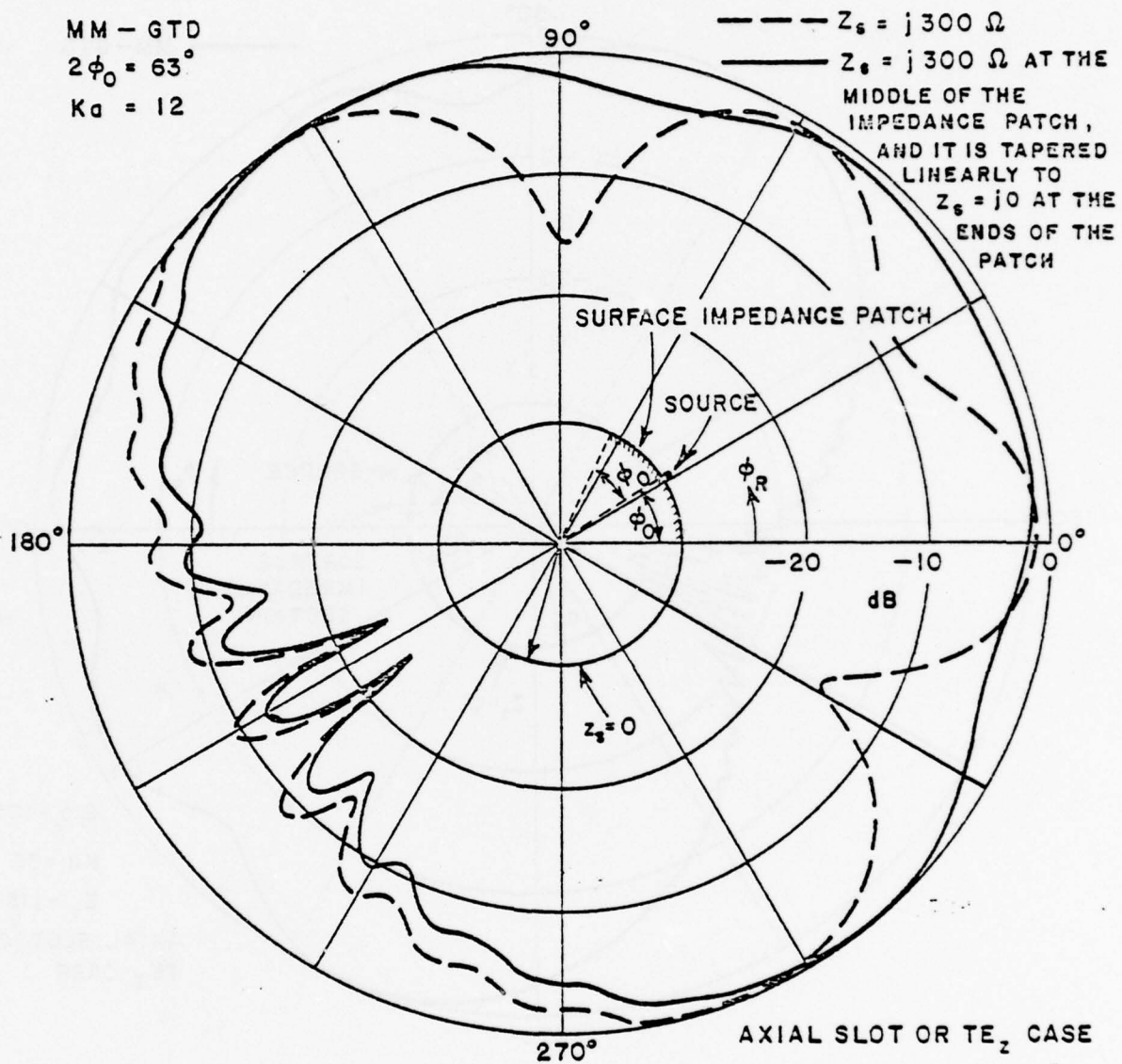


Figure 16. Radiation pattern of a magnetic line source on a perfectly-conducting circular cylinder which is covered with an impedance surface patch.

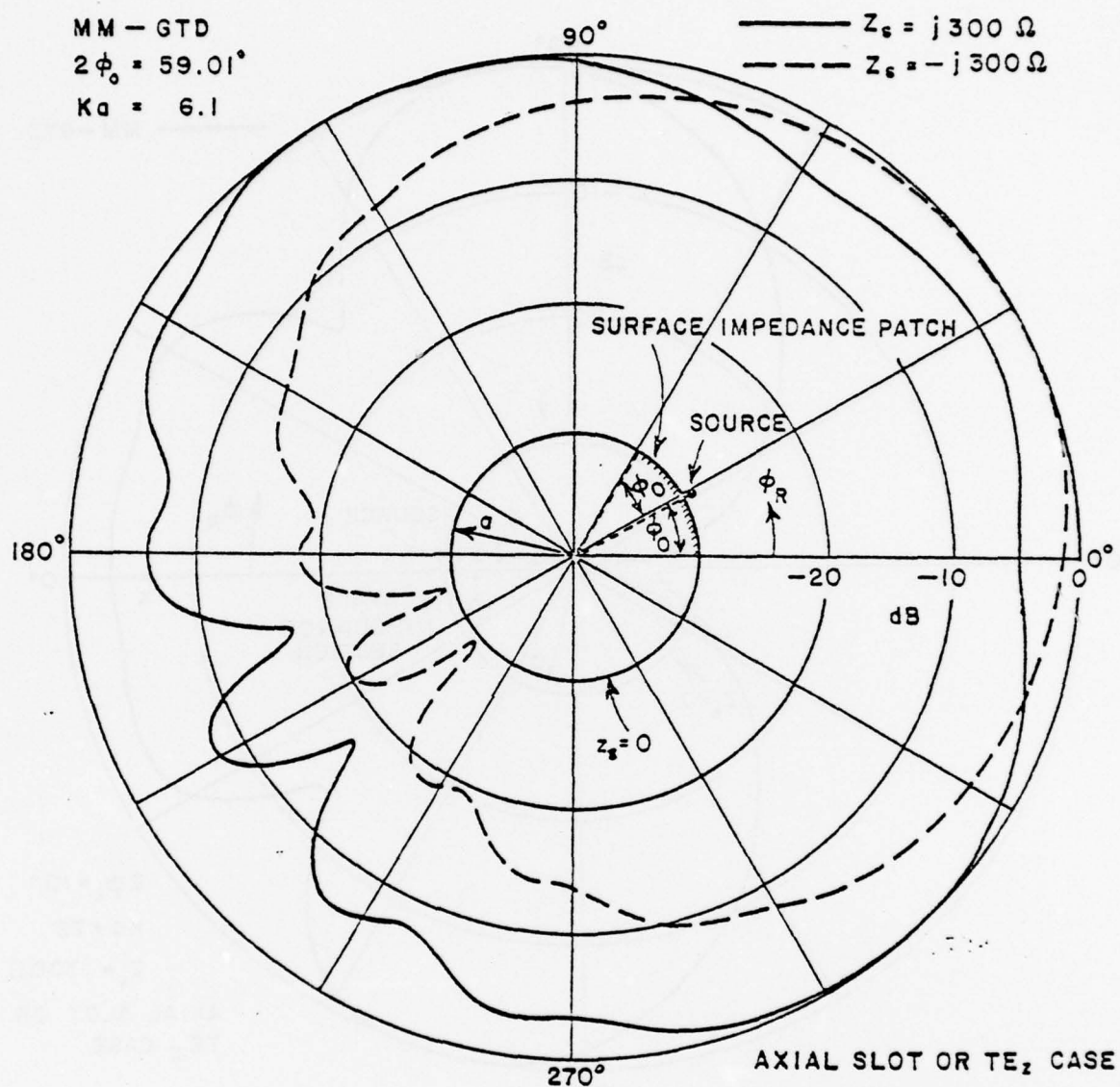


Figure 17. Radiation pattern of a magnetic line source on a perfectly-conducting circular cylinder which is covered with an impedance surface patch.

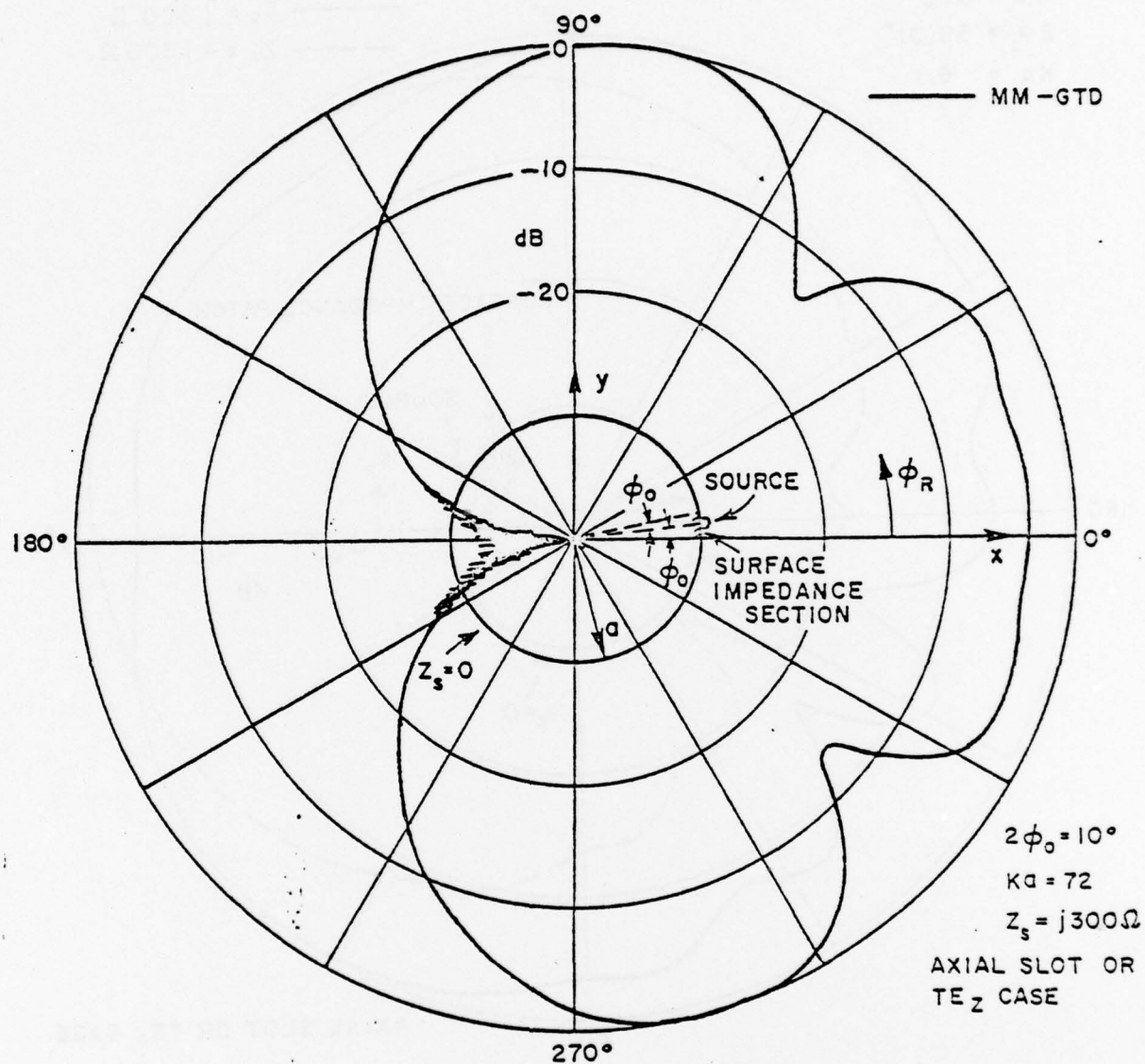


Figure 18. Radiation pattern of a magnetic line source on a perfectly-conducting circular cylinder which is covered with an impedance surface patch.

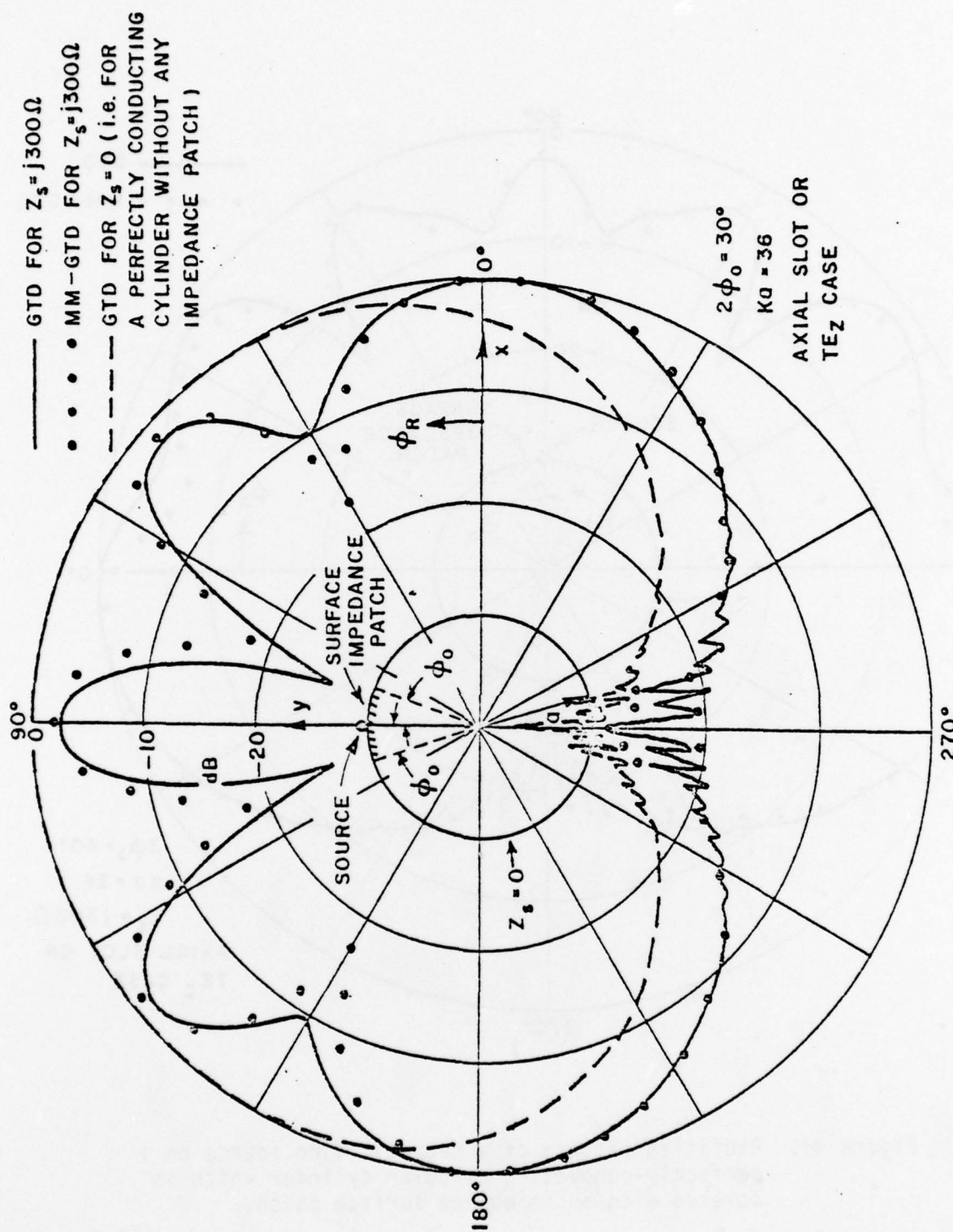


Figure 19. Radiation pattern of a magnetic line source on a perfectly-conducting circular cylinder which is covered with an impedance surface patch.

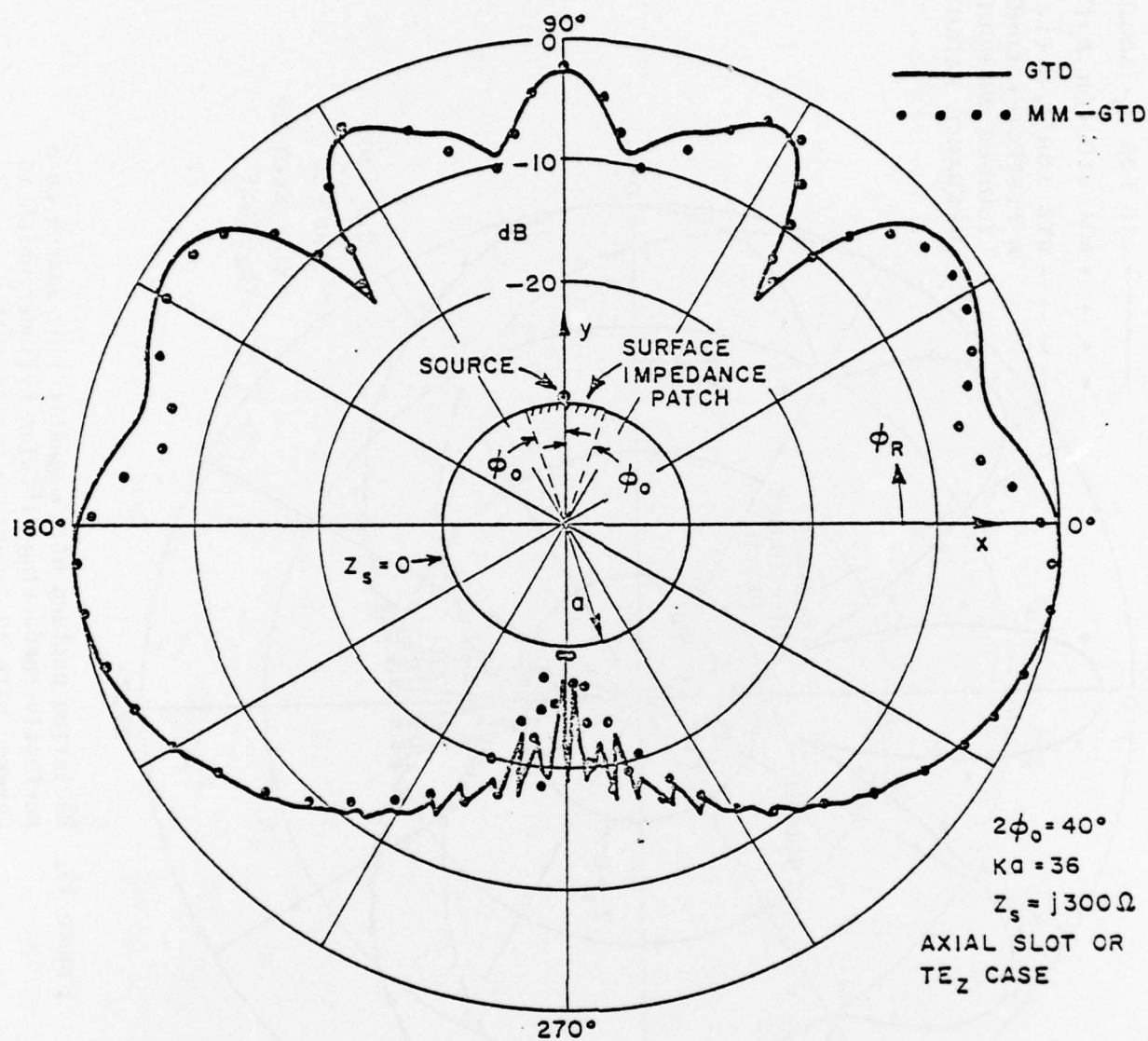


Figure 20. Radiation pattern of a magnetic line source on a perfectly-conducting circular cylinder which is covered with an impedance surface patch.

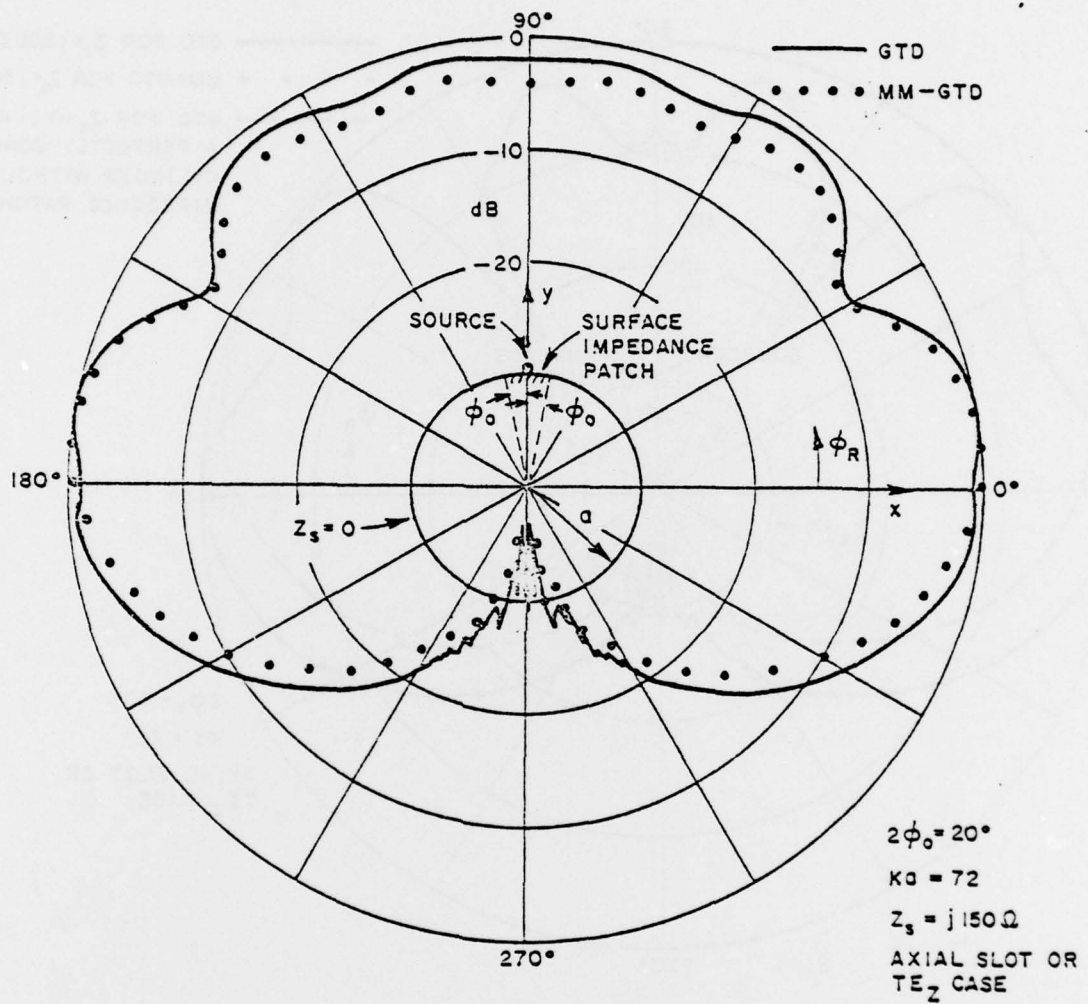


Figure 21. Radiation pattern of a magnetic line source on a perfectly-conducting circular cylinder which is covered with an impedance surface patch.

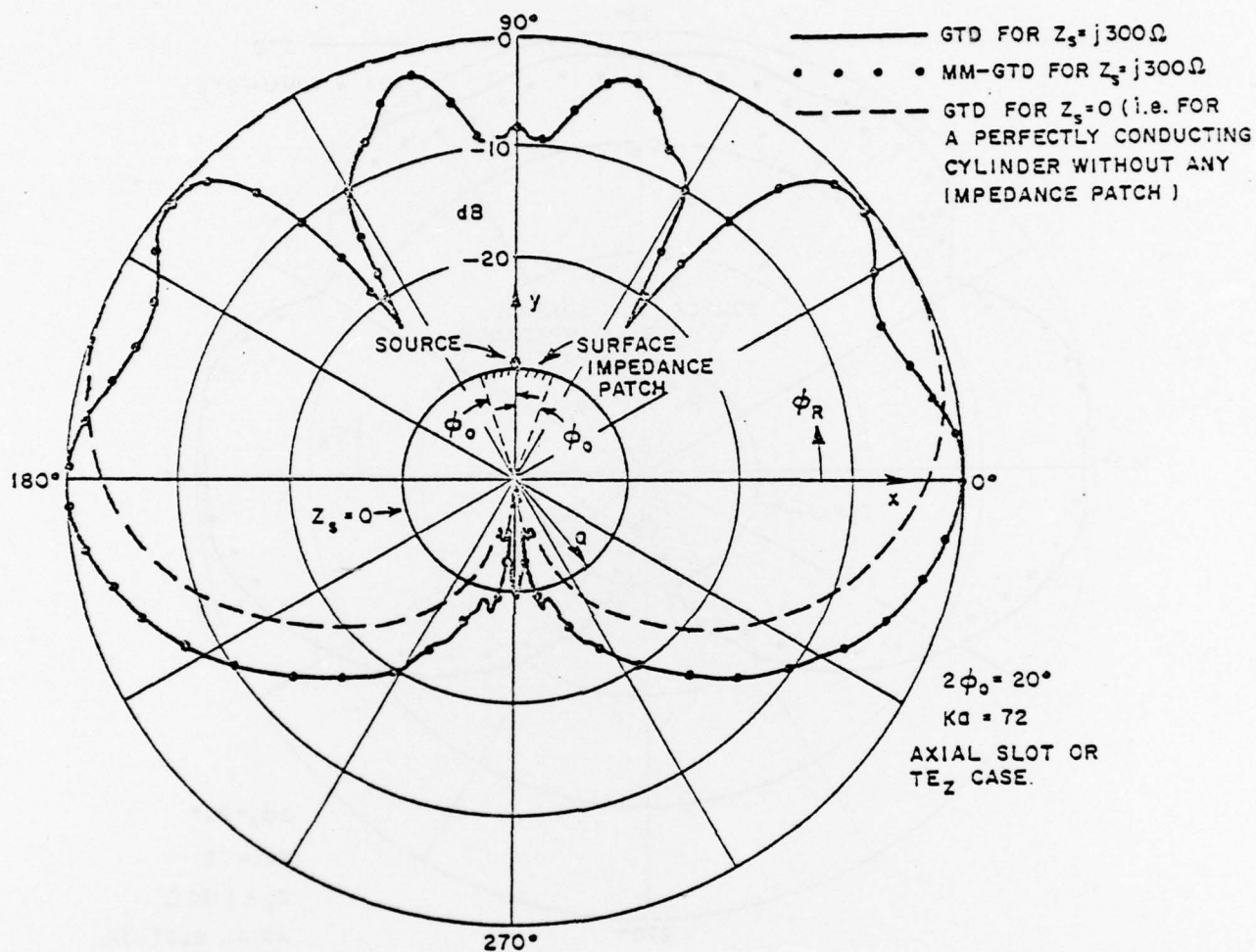


Figure 22. Radiation pattern of a magnetic line source on a perfectly-conducting circular cylinder which is covered with an impedance surface patch.

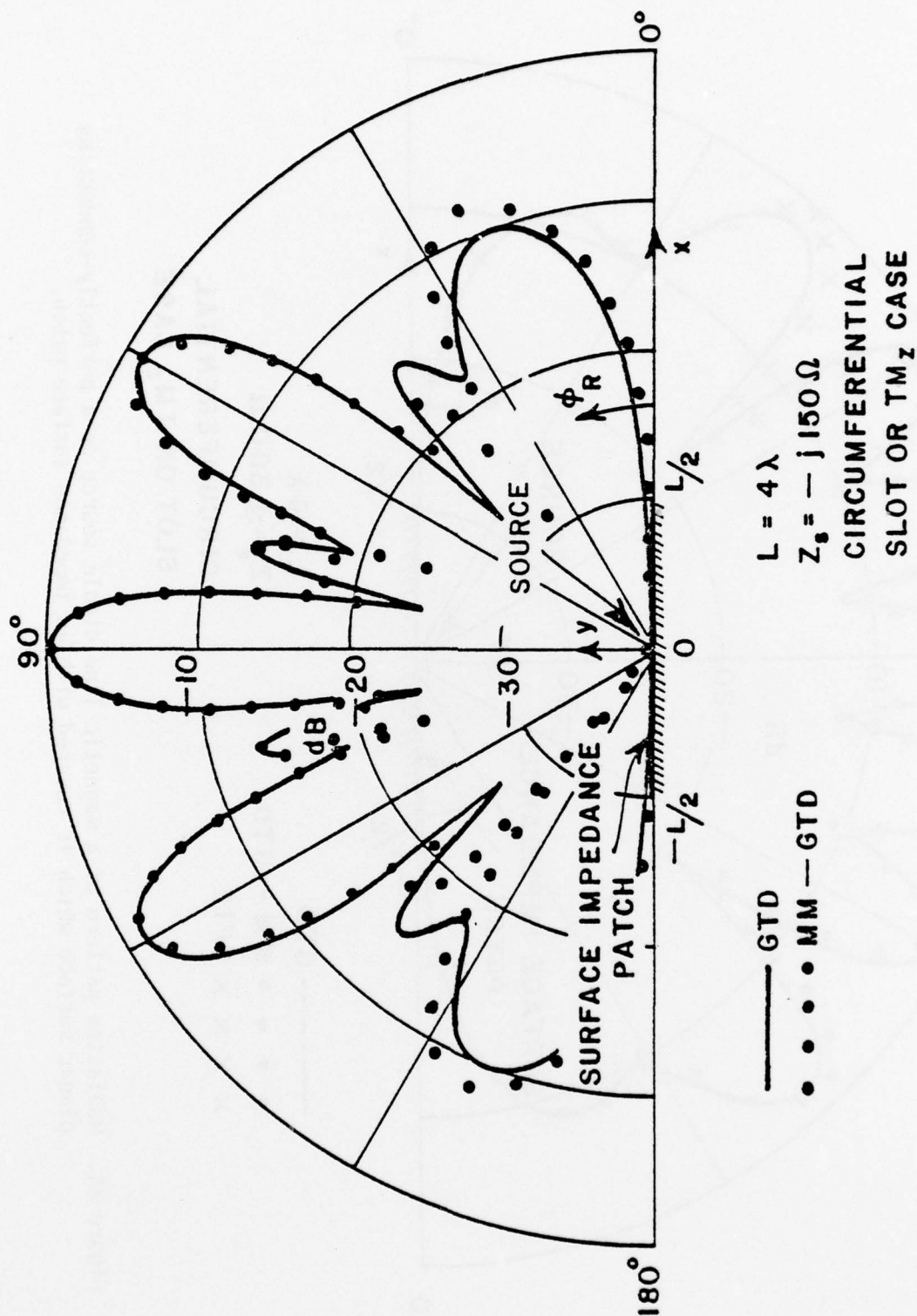


Figure 23. Radiation pattern of a magnetic line dipole source on a perfectly-conducting planar surface which is covered with an impedance surface patch.

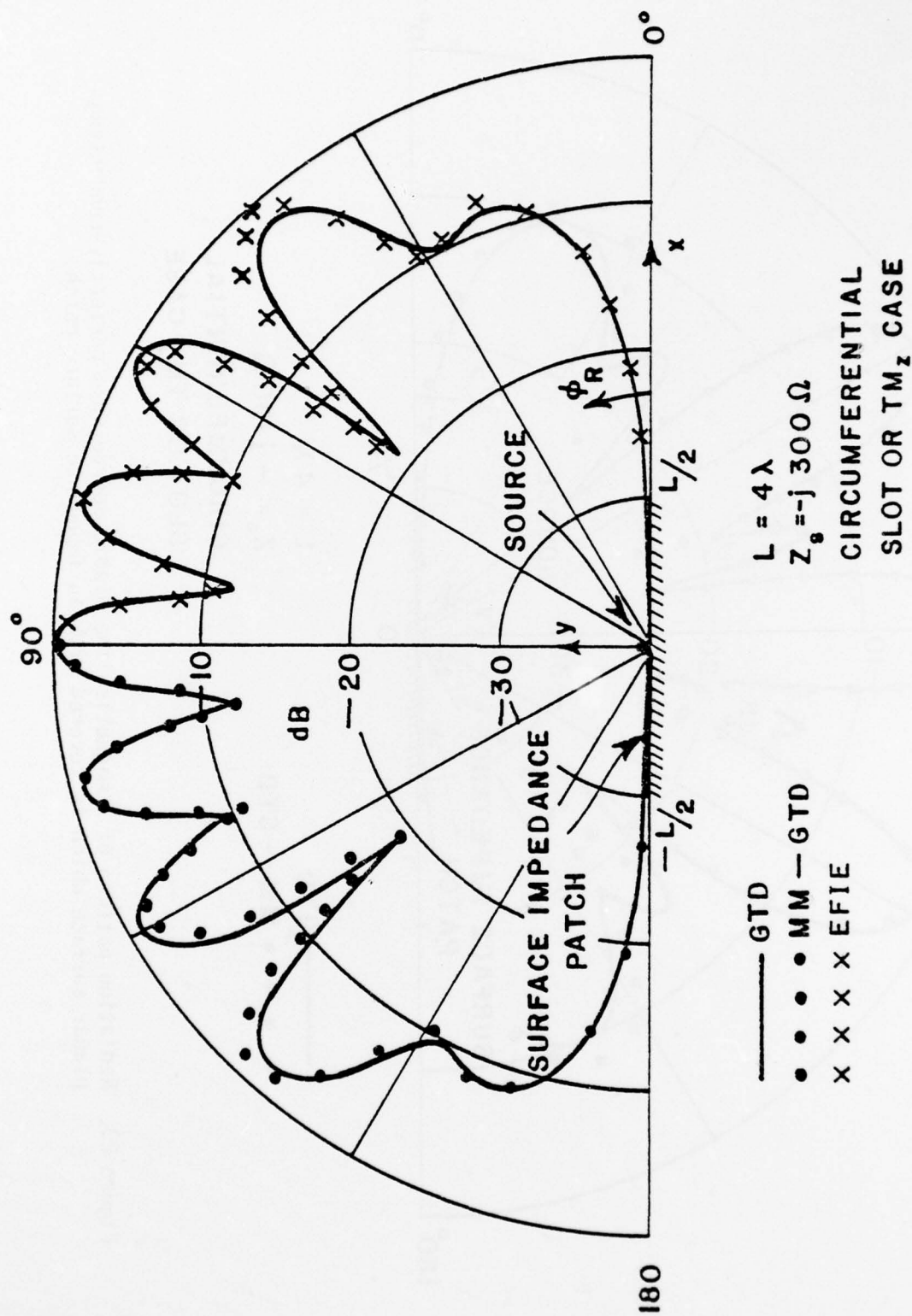


Figure 24. Radiation pattern of a magnetic line dipole source on a perfectly-conducting planar surface which is covered with an impedance surface patch.

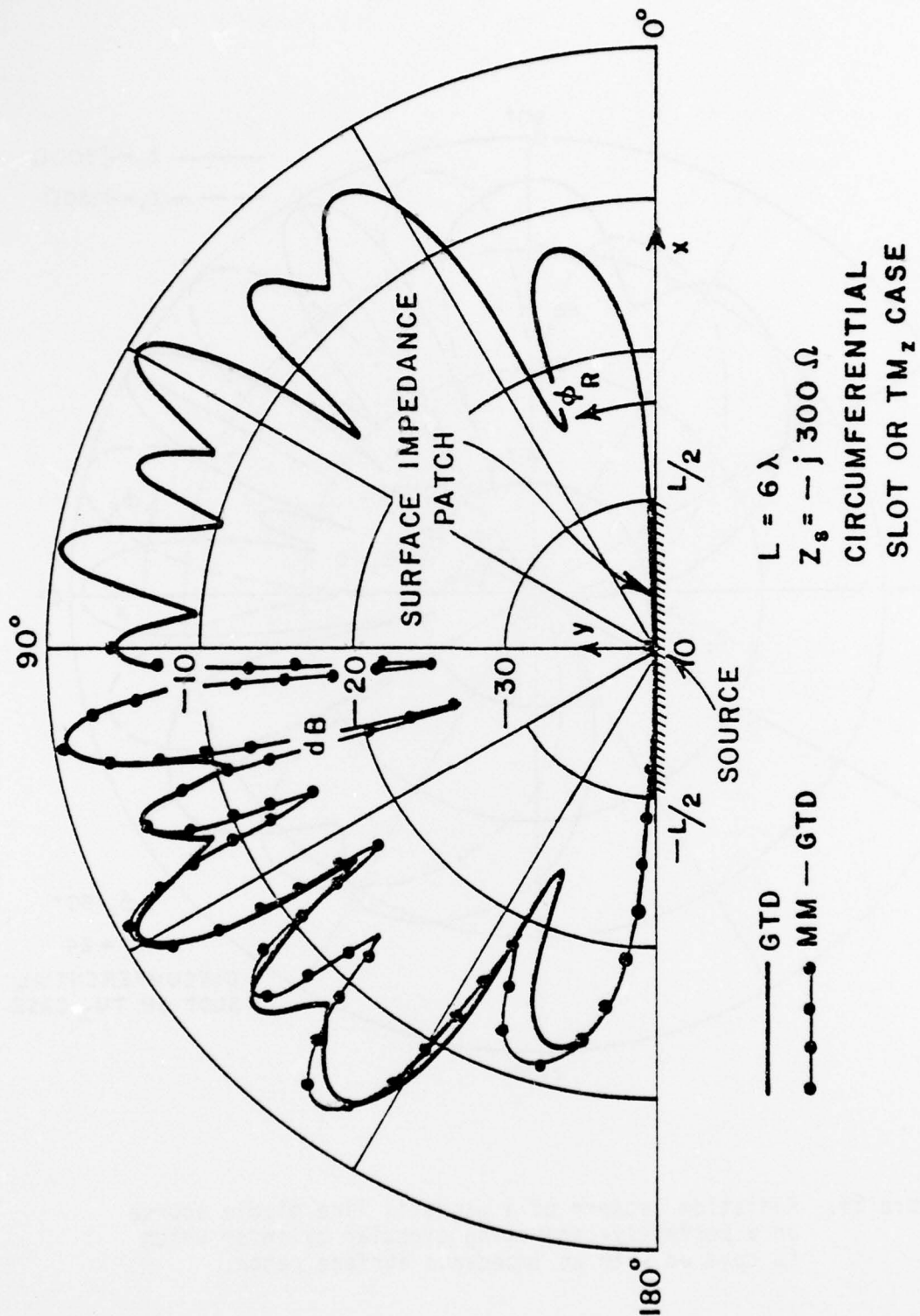


Figure 25. Radiation pattern of a magnetic line dipole source on a perfectly-conducting planar surface which is covered with an impedance surface patch.

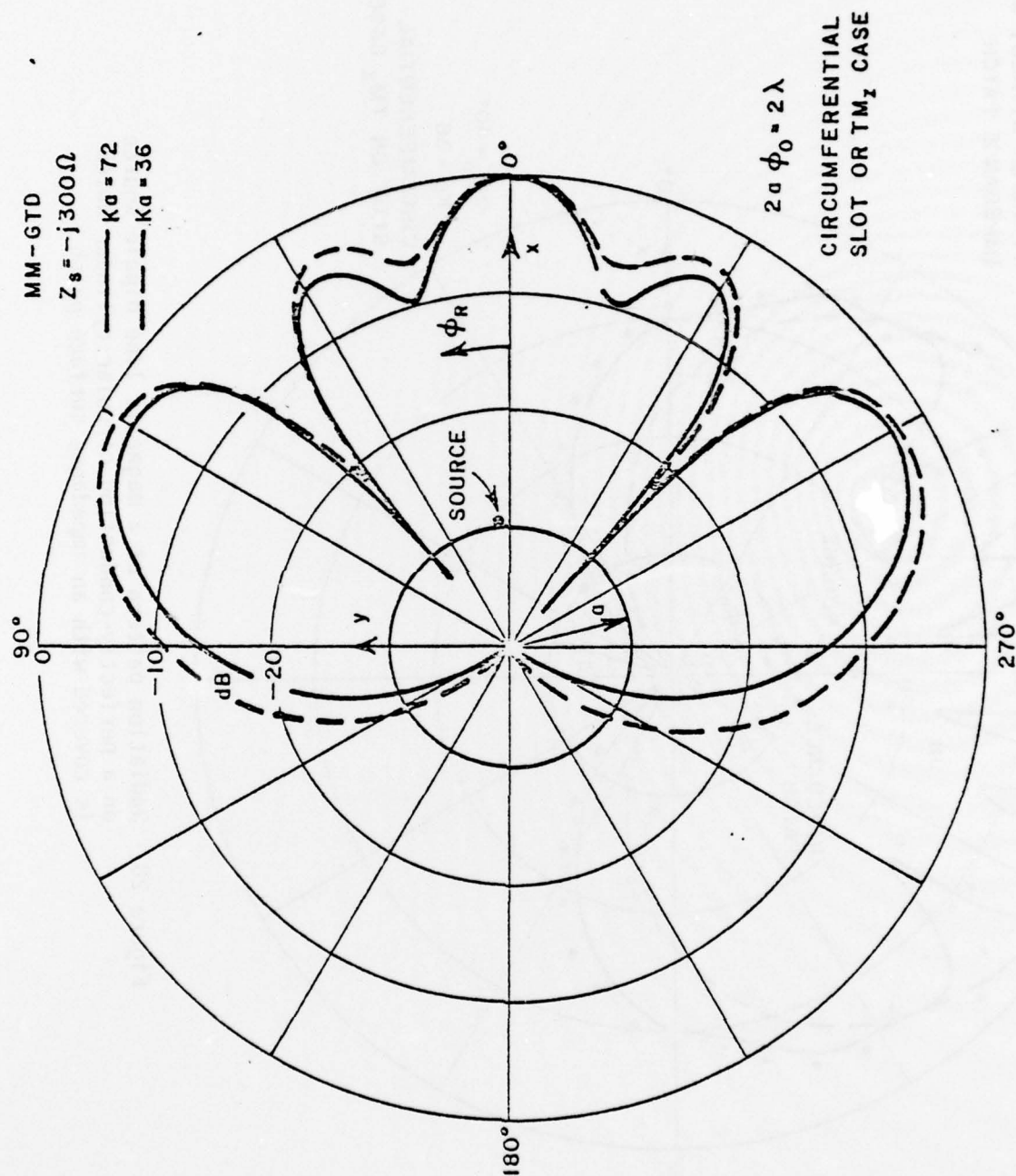


Figure 27. Radiation pattern of a magnetic line dipole source on a perfectly-conducting circular cylinder which is covered with an impedance surface patch.

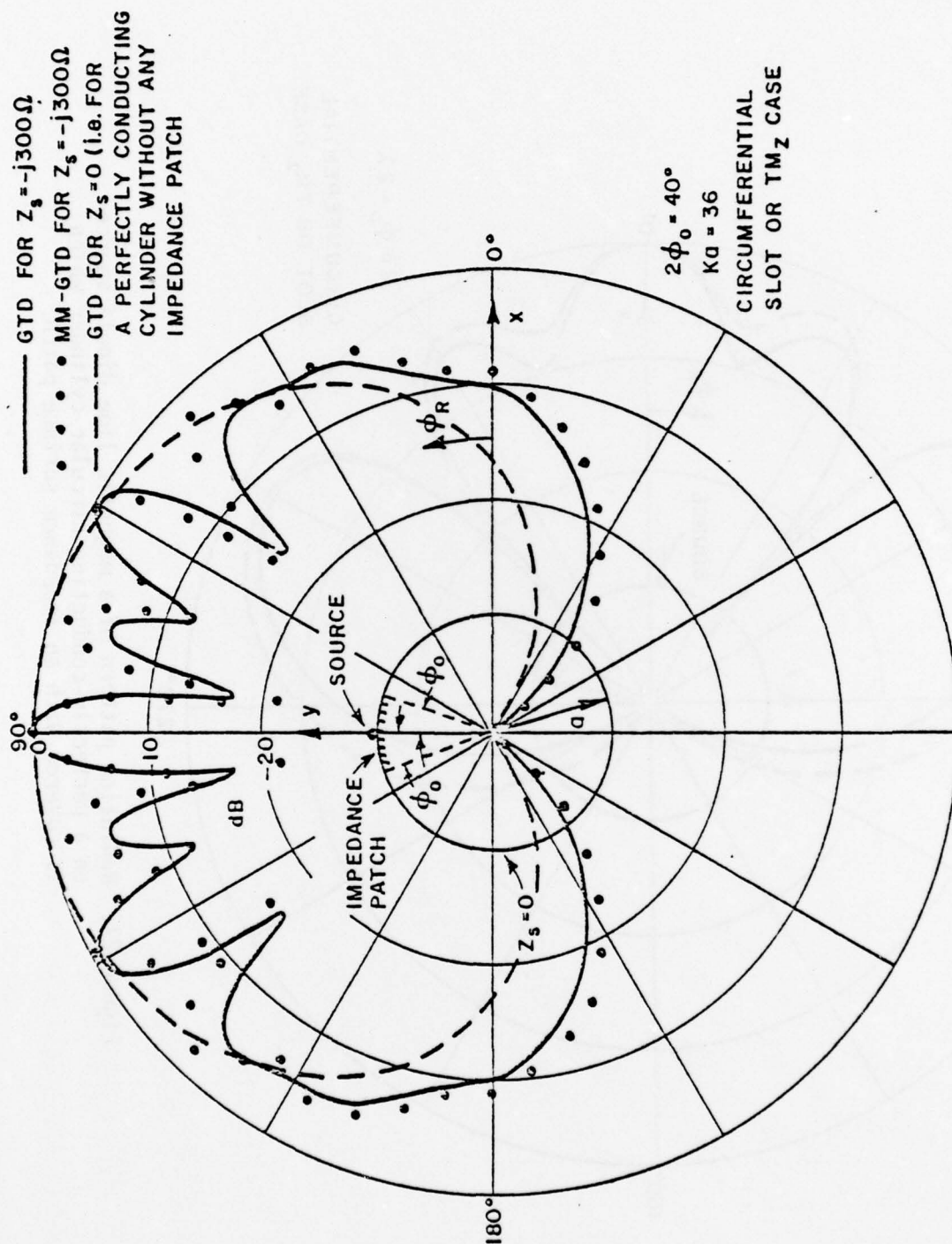


Figure 28. Radiation pattern of a magnetic line dipole source on a perfectly-conducting circular cylinder which is covered with an impedance surface patch.

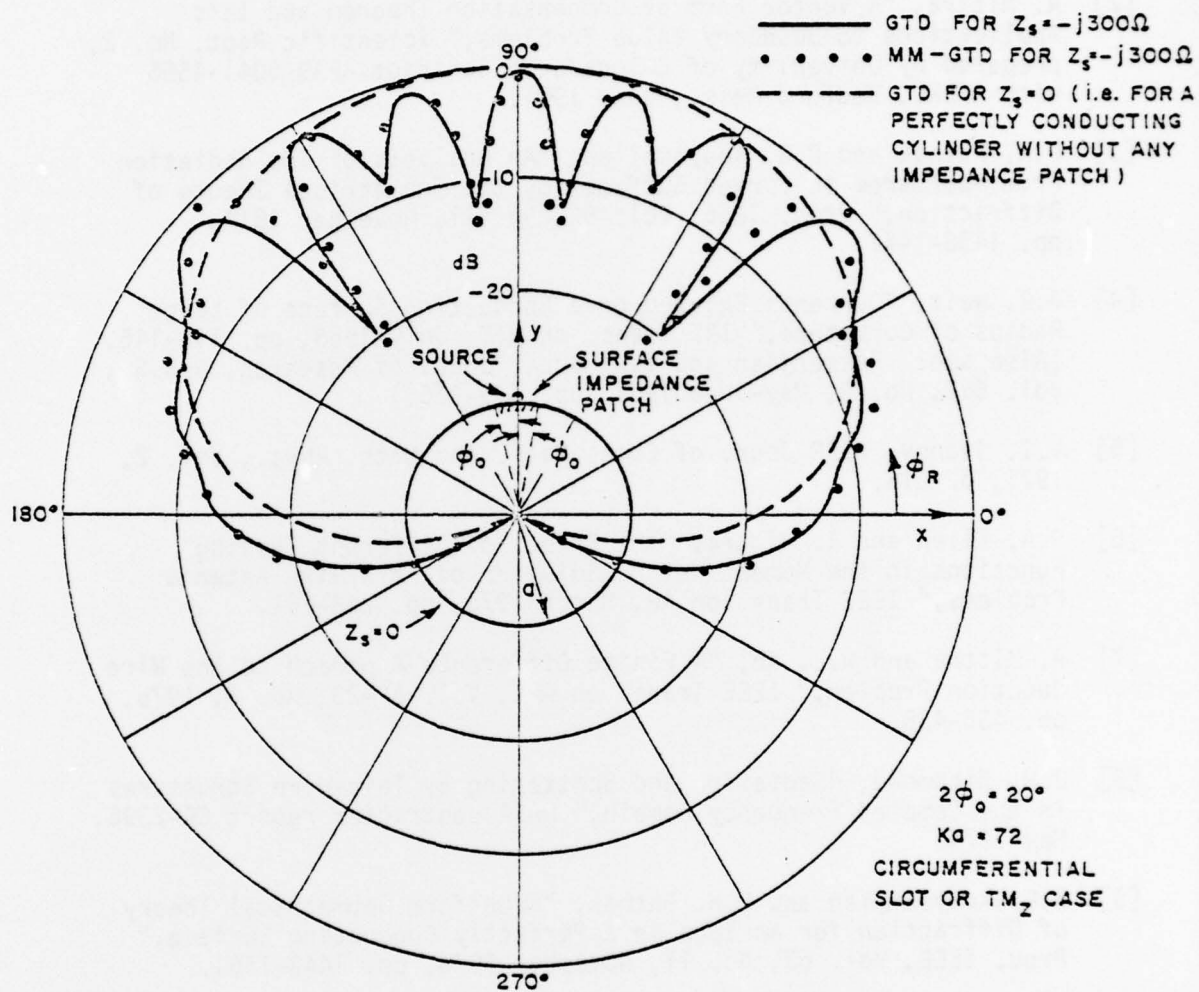


Figure 29. Radiation pattern of a magnetic line dipole source on a perfectly-conducting circular cylinder which is covered with an impedance surface patch.

REFERENCES

- [1] R.S. Elliot, "Azimuthal Surface Waves on Circular Cylinders," Jour. of Appl. Phys., Vol. 26, No. 4, April 1955, pp. 368-376.
- [2] R. Mittra, "A Vector Form of Compensation Theorem and It's Applications to Boundary Value Problems," Scientific Rept. No. 2, prepared by University of Colorado on Contract AF19(604)-4556 with AFCRL, Bedford Mass., June 1961.
- [3] P.H. Pathak and R.G. Kouyoumjian, "An Analysis of The Radiation From Apertures in Curved Surfaces by the Geometrical Theory of Diffraction," Proc. IEEE, Vol. 62, No. 11, November 1974, pp. 1438-1447.
- [4] J.R. Wait, "Currents Excited on a Conducting Surface of Large Radius of Curvature," IRE Trans. on MTT, July 1956, pp. 143-145. (Also see: Hasserjian and Ishimaru, "Jour. of Research, N.B.S., Vol. 66D, No. 3, May-June 1962, pp. 335-365.)
- [5] V.I. Ivanov, USSR Jour. of Comp. Math. and Math. Phys., Vol. 2, 1971, p. 216.
- [6] C.A. Klien and R. Mittra, "The Effect of Different Testing Functions in the Moment Method Solution of Thin Wire Antenna Problems," IEEE Trans. on AP, March 1975, pp. 258-261.
- [7] R. Mittra and W.L. Ko, "A Finite Difference Approach to the Wire Junction Problem," IEEE Trans. on AP., Vol. AP-23, No. 3, 1975, pp. 435-438.
- [8] J.H. Richmond, "Radiation and Scattering by Thin-Wire Structures in the Complex Frequency Domain," NASA contractor report CR-2396, May 1974.
- [9] R.G. Kouyoumjian and P.H. Pathak, "A Uniform Geometrical Theory of Diffraction for an Edge in a Perfectly Conducting Surface," Proc. IEEE, Vol. 62, No. 11, November 1974, pp. 1448-1461.
- [10] W.D. Burnside, M.C. Gilreath, R.J. Marhefka and C.L. Yu, "A Study of KC-135 Aircraft Antenna Pattern," IEEE Trans. AP, May 1975, pp. 309-316.
- [11] P.H. Pathak, "A GTD Analysis of the Radiation From Slots in Planar and Cylindrical Perfectly-Conducting Structures with a Surface Impedance Patch," Final Report 4396-2, The Ohio State University ElectroScience Laboratory, Department of Electrical Engineering; in preparation under Contract F19628-76-C-0154 for Department of the Air Force, Electronic Systems Division, Hanscom Air Force Base, Mass. 01731.

METRIC SYSTEM

BASE UNITS:

Quantity	Unit	SI Symbol	Formula
length	metre	m	...
mass	kilogram	kg	...
time	second	s	...
electric current	ampere	A	...
thermodynamic temperature	kelvin	K	...
amount of substance	mole	mol	...
luminous intensity	candela	cd	...

SUPPLEMENTARY UNITS:

plane angle	radian	rad	...
solid angle	steradian	sr	...

DERIVED UNITS:

Acceleration	metre per second squared	...	m/s
activity (of a radioactive source)	disintegration per second	...	(disintegration)/s
angular acceleration	radian per second squared	...	rad/s
angular velocity	radian per second	...	rad/s
area	square metre	...	m
density	kilogram per cubic metre	...	kg/m
electric capacitance	farad	F	A·s/V
electrical conductance	siemens	S	A/V
electric field strength	volt per metre	...	V/m
electric inductance	henry	H	V·s/A
electric potential difference	volt	V	W/A
electric resistance	ohm	...	V/A
electromotive force	volt	V	W/A
energy	joule	J	N·m
entropy	joule per kelvin	...	J/K
force	newton	N	kg·m/s
frequency	hertz	Hz	(cycle)/s
illuminance	lux	lx	lm/m
luminance	candela per square metre	...	cd/m
luminous flux	lumen	lm	cd·sr
magnetic field strength	ampere per metre	...	A/m
magnetic flux	weber	Wb	V·s
magnetic flux density	tesla	T	Wb/m
magnetomotive force	ampere	A	...
power	watt	W	J/s
pressure	pascal	Pa	N/m
quantity of electricity	coulomb	C	A·s
quantity of heat	joule	J	N·m
radiant intensity	watt per steradian	...	W/sr
specific heat	joule per kilogram-kelvin	...	J/kg·K
stress	pascal	Pa	N/m
thermal conductivity	watt per metre-kelvin	...	W/m·K
velocity	metre per second	...	m/s
viscosity, dynamic	pascal-second	...	Pa·s
viscosity, kinematic	square metre per second	...	m/s
voltage	volt	V	W/A
volume	cubic metre	...	m
wavenumber	reciprocal metre	...	(wave)/m
work	joule	J	N·m

SI PREFIXES:

Multiplication Factors	Prefix	SI Symbol
1 000 000 000 000 = 10 ¹²	tera	T
1 000 000 000 = 10 ⁹	giga	G
1 000 000 = 10 ⁶	mega	M
1 000 = 10 ³	kilo	k
100 = 10 ²	hecto*	h
10 = 10 ¹	deka*	da
0.1 = 10 ⁻¹	deci*	d
0.01 = 10 ⁻²	centi*	c
0.001 = 10 ⁻³	milli	m
0.000 001 = 10 ⁻⁶	micro	μ
0.000 000 001 = 10 ⁻⁹	nano	n
0.000 000 000 001 = 10 ⁻¹²	pico	p
0.000 000 000 000 001 = 10 ⁻¹⁵	femto	f
0.000 000 000 000 000 001 = 10 ⁻¹⁸	atto	a

* To be avoided where possible.